

Detachment faulting in a bivergent core complex constrained by fault gouge dating and low-temperature thermochronology

Caroline Heineke^a, Ralf Hetzel^{a,*}, Nils-Peter Nilius^b, Horst Zwingmann^c, Andrew Todd^d, Andreas Mulch^{e,f}, Andreas Wölfler^b, Christoph Glotzbach^g, Cüneyt Akal^h, István Dunklⁱ, Mark Raven^j, Andrea Hampel^b

^a Institut für Geologie und Paläontologie, Westfälische Wilhelms-Universität Münster, Corrensstraße 24, D-48149, Münster, Germany

^b Institut für Geologie, Leibniz Universität Hannover, Callinstraße 30, D-30167, Hannover, Germany

^c Department of Geology and Mineralogy, Kyoto University, Kitashirakawa Oiwake-cho, 606-8502, Kyoto, Japan

^d CSIRO Energy, 26 Dick Perry Ave, Kensington, WA 6151, Australia

^e Senckenberg Biodiversity and Climate Research Centre (BiK-F), Senckenberganlage 25, D-60325, Frankfurt, Germany

^f Institut für Geowissenschaften, Goethe-Universität Frankfurt, Altenhöferallee 1, 60438, Frankfurt, Germany

^g Department of Geosciences, University of Tübingen, Wilhelmstraße 56, D-72074, Tübingen, Germany

^h Dokuz Eylül University, Engineering Faculty, Department of Geological Engineering, Tinaztepe Campus, Buca, TR-35390, Izmir, Turkey

ⁱ Geowissenschaftliches Zentrum der Universität Göttingen, Abteilung Sedimentologie/Umweltgeologie, Goldschmidtstraße 3, D-37077, Göttingen, Germany

^j CSIRO Land and Water, Waite Road, Urrbrae, SA, 5064, Australia



ARTICLE INFO

Keywords:

Fault gouge
K-Ar dating
Detachment faulting
Thermochronology
Hydrogen isotopes
Menderes massif

ABSTRACT

The central Menderes Massif in western Turkey is a bivergent metamorphic core complex characterised by two detachment faults that operated with opposite sense of shear. Here, we present K-Ar ages and hydrogen isotope data for fault gouge as well as fission track and (U-Th)/He ages for apatite and zircon from bedrock samples to constrain the timing of detachment faulting. Comparison of the K-Ar ages and low-temperature thermochronologic ages indicates brittle faulting at temperatures between ~240 and ~70 °C. At the western termination of the Gediz detachment, K-Ar ages between ~12 and ~5 Ma suggest rather continuous faulting since the mid-Miocene; a Pliocene phase of rapid slip is mainly recorded in the eastern part of this detachment. In contrast, K-Ar ages from the Büyükk Menderes detachment cluster at 22–16 and 9–3 Ma and provide evidence for two phases of faulting, which is in accordance with new and published low-temperature thermochronologic data. Hydrogen isotope ratios of ~76 to ~115‰ indicate infiltration of meteoric water during detachment faulting and gouge formation. The youngest K-Ar ages and cooling histories for hanging and footwall rocks imply that the activity of both detachments ended ~3 Ma ago when the currently active grabens were established.

1. Introduction

Brittle faulting accommodates much of the deformation in the Earth's upper crust and is a key process that governs landscape evolution in tectonically active regions. In order to understand how landscapes evolve in response to crustal shortening or extension, it is crucial to constrain the timing of brittle faulting episodes. Commonly, this is done indirectly by applying low-temperature thermochronology to the hanging wall and footwall of thrust or normal faults and by thermo-kinematic modelling of the respective cooling paths to account for heat advection and to quantify slip-rate histories (e.g. Thiede et al., 2005; Campani et al., 2010; Braun et al., 2012; McCallister et al., 2014; Wolff et al., 2019). In contrast, direct dating of brittle fault rocks such as

breccia, cataclasite, fault gouge, or pseudotachylite (e.g. Eide et al., 1997; Sherlock and Hetzel, 2001; van der Pluijm et al., 2001; Zwingmann and Mancktelow, 2004; Wölfler et al., 2010; Ault et al., 2015) is more challenging due to the fine-grained nature of most fault rocks. Against this background, the direct dating of brittle faults combined with low-temperature thermochronology is a particularly valuable approach to decipher the timing of brittle deformation phases (e.g. Duvall et al., 2011; Mancktelow et al., 2016; Ring et al., 2017).

Probably the most common rock type that forms during brittle faulting and cataclasis is clay-rich fault gouge, which typically contains the K-bearing mineral illite. The pioneering studies of Lyons and Snellenburg (1971) and Kralik et al. (1987) have shown the great potential of K-Ar and Rb-Sr dating of clay fractions from fault gouge in

* Corresponding author.

E-mail address: rahetzel@uni-muenster.de (R. Hetzel).

order to determine the age of faulting. Since then, an increasing number of studies has employed K–Ar and ^{40}Ar - ^{39}Ar dating of synkinematic illite from fault gouge to provide absolute age constraints on brittle faulting (e.g. Vrolijk and van der Pluijm, 1999; Choo and Chang, 2000; Haines and van der Pluijm, 2008; Zwingmann et al., 2010, 2011; Rahl et al., 2011; Haines et al., 2016).

The combination of absolute fault gouge dating with low-temperature thermochronology has often been applied to characterise the activity of low-angle normal faults in extensional tectonic settings (e.g. Haines and van der Pluijm, 2012; Mancktelow et al., 2016). Such low-angle normal or detachment faults are a general feature of metamorphic core complexes that form during the syn-, late-, or post-orogenic extension of mountain belts (e.g. Dewey, 1988; Lister and Davis, 1989; Burchfiel et al., 1992; Malavieille, 1993; Singleton et al., 2014). Detachment faults, which represent the upward continuation of ductile shear zones, accommodate large amounts of extension and are responsible for the rapid exhumation of metamorphic rocks from mid-crustal depth (e.g. Crittenden et al., 1980; Forsyth, 1992). Regarding the geometry and kinematics of core complexes and detachment faults, two end-member types can be distinguished (Malavieille, 1993). The more common type is asymmetric and bounded by a single detachment (e.g. Wernicke and Axen, 1988; Lister and Davis, 1989). The other type is characterised by bivergent extension, which is accommodated by detachment faults with opposing dip directions on both flanks of the core complex (Malavieille, 1993; Faure et al., 1996; Vanderhaeghe et al., 1999; Gessner et al., 2001). Typical processes that occur during the evolution of metamorphic core complexes are the overprinting of older mylonitic fabrics by younger cataclastic fault zones and discrete brittle faults (e.g. Crittenden et al., 1980; Lister and Davis, 1989) and the infiltration of meteoric fluids into the detachment faults, as shown by stable isotope studies (e.g. Fricke et al., 1992; Caine et al., 1996; Mulch and Chamberlain, 2007; Gébelin et al., 2015).

Here, we present 19 new K–Ar ages to constrain the age of detachment faulting in a key area of continental extension: the Menderes Massif in Western Turkey. The central part of this massif constitutes a bivergent metamorphic core complex that was exhumed by slip on two detachment faults with opposite dip and sense of shear. Our K–Ar ages, complemented by new and previously published low-temperature thermochronologic data, allow us to evaluate if the two detachment faults were active simultaneously or not. In addition, the hydrogen isotope composition of the dated fault gouge samples was measured to test if meteoric fluids have infiltrated the detachment faults during periods of fault activity.

2. The central Menderes Massif

Since ~ 25 Ma, the Aegean region in the back-arc of the Hellenic subduction zone has experienced pronounced extensional deformation, which resulted in the exhumation of mid-crustal rocks exposed in numerous metamorphic massifs and core complexes (e.g. McKenzie, 1978; Jolivet and Faccenna, 2000; Brun and Sokoutis, 2010; Jolivet et al., 2013). The Menderes Massif in western Turkey is one of the largest of these metamorphic massifs. It is cut by two active E–W trending grabens – the Gediz and Büyük Menderes grabens – which subdivide the massif into three submassifs (e.g. Seyitoğlu and Scott, 1991; Yılmaz et al., 2000; Gürer et al., 2009) and bound the central Menderes Massif in the north and south (Fig. 1).

The metamorphic rocks of the central Menderes Massif comprise four nappes that were stacked during late Cretaceous to Eocene plate convergence along the Izmir-Ankara suture zone (e.g. Sengör et al., 1984; Ring et al., 1999; van Hinsbergen et al., 2010; Gessner et al., 2013). From lowest to highest structural level, these nappes include the Bayındır, Bozdağı, Çine, and Selimiye nappes, which are structurally overlain by the Cycladic blueschist unit in the west (Ring et al., 1999; Gessner et al., 2013) (Fig. 1). The Bozdağı, Bayındır, and Selimiye nappes consist mainly of greenschist to amphibolite facies mica schists,

quartzites and phyllites; the two latter also contain some marbles (Dora et al., 1990; Hetzel et al., 1998; Özer and Sözbilir, 2003; Candan et al., 2011). The Çine nappe consists largely of orthogneisses and pelitic gneisses (e.g. Hetzel and Reischmann, 1996; Hetzel et al., 1998; Candan et al., 2001). At the northern and southern margins of the central Menderes Massif two belts of Neogene sedimentary rocks are well exposed due to ongoing footwall uplift along the active boundary faults of the Gediz and Büyük Menderes grabens (Fig. 1).

The Küçük Menderes Graben separates the central Menderes Massif into the Bozdağı and Aydin mountain ranges, which are bounded by shallow-dipping detachment faults (Fig. 1). The central Menderes Massif was exhumed during bivergent N–S-directed extension on these two faults and thus constitutes a symmetric core complex (Gessner et al., 2001). The rocks in the footwall of the Gediz detachment, at the northern slope of the Bozdağı Range, exhibit a top-to-the-N to NNE sense of shear (Hetzel et al., 1995), whereas the shear sense of the Büyük Menderes detachment was opposite, i.e. top-to-the-S to SSW (Emre, 1996; Gessner et al., 2001; Işık et al., 2003). As both detachments cut obliquely through the nappe pile, the structurally higher Çine nappe was emplaced against the lower Bayındır nappe. Therefore, orthogneisses of the Çine nappe occur as klippen above the two detachments (Fig. 1) (Hetzel et al., 1995; Buscher et al., 2013; Wölfle et al., 2017). Likewise, the Neogene sedimentary rocks along the northern and southern margins of the massif were tectonically emplaced on the detachment faults during progressive extension and normal faulting. Finally, both detachment faults were cut by the high-angle boundary faults of the Gediz and Büyük Menderes grabens.

The timing of detachment faulting in the central Menderes Massif has hitherto been inferred from different types of geochronological data but is still not well resolved. At the Gediz detachment, ductile deformation and normal faulting was initially interpreted to have been underway in the mid-Miocene, based on U–Pb zircon ages of ~ 16 – 15 Ma and ^{40}Ar - ^{39}Ar plateau ages of ~ 13 – 12 Ma for biotite from two synextensive intrusions, the Turgutlu and Salihli granodiorites (Hetzel et al., 1995; Glodny and Hetzel, 2007) (Fig. 1). More recently, *in situ* U–(Th)–Pb dating of titanite from the Salihli granodiorite was used to suggest that the pre-extensional emplacement and crystallization of the magma occurred at 17–16 Ma, whereas ductile extensional deformation began 1–2 Ma later at 15–14 Ma (Rossetti et al., 2017). ^{40}Ar - ^{39}Ar laser dating of synkinematic white mica from one mylonite sample beneath the Gediz detachment yielded two single-fusion ages of 6.6 ± 2.5 and 6.7 ± 1.1 Ma (weighted mean: 6.7 ± 1.0 Ma), indicating ongoing deformation at temperatures near the brittle–ductile transition zone in the latest Miocene (Lips et al., 2001). The first few apatite and zircon fission track ages from the central Menderes Massif were interpreted to indicate that both the Gediz and Büyük Menderes detachments were active simultaneously, with a period of particularly rapid cooling in the Pliocene (Gessner et al., 2001; Ring et al., 2003). The latter phase of extension was also inferred from an ion microprobe Th–Pb age of 4.5 ± 1.0 Ma for retrograde monazite from the Salihli granodiorite (Catlos and Çemen, 2005). This period of fast cooling and exhumation in the eastern part of the Gediz detachment took place between ~ 4 and ~ 2 Ma as shown by a detailed thermochronologic study of the Salihli granodiorite (Buscher et al., 2013). At the Büyük Menderes detachment, a similar study revealed two distinct phases of cooling in the middle Miocene and latest Miocene/Pliocene (Wölfle et al., 2017), which have been confirmed by additional data taken along strike of the detachment fault (Nilius et al., 2019). A first attempt to use K–Ar dating of fault gouge and cataclasite to provide direct age constraints on brittle faulting yielded ages of 10–9 Ma and 4–3 Ma near the eastern end of the Gediz detachment and ages of ~ 22 Ma and ~ 5 – 3 Ma at the Büyük Menderes detachment (Hetzel et al., 2013; for location of samples see Fig. 1).

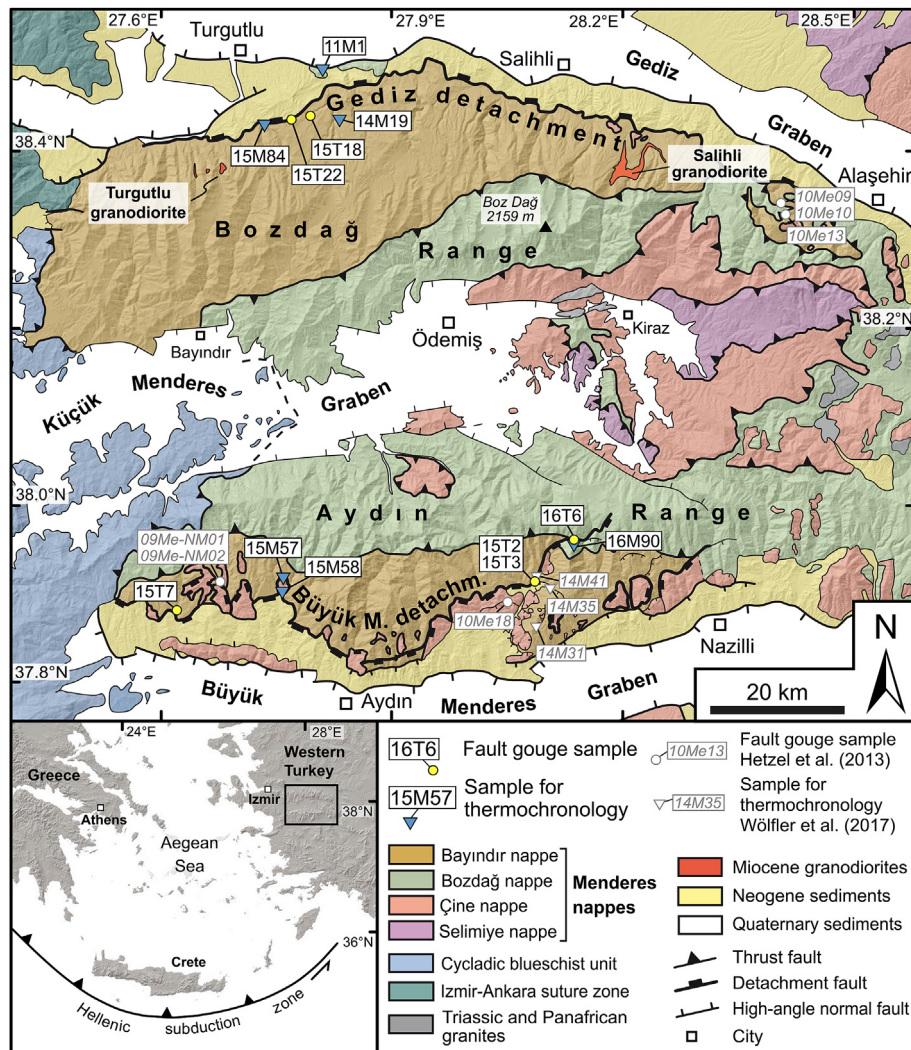


Fig. 1. Geological map of the central Menderes Massif (modified from Wöfler et al., 2017 and complemented with own field observations). Note that samples 15M57, 15M58, and 16M90 are included in Nilius et al. (2019). Map in lower left part of figure shows the location of the study area within the Aegean region.

3. Sampling sites and sample description

To better constrain the timing of detachment faulting in the central Menderes Massif, we collected six fault gouge samples for K-Ar dating at five new sites of the Gediz and Büyük Menderes detachment faults (Fig. 1). At all sites, we used hammer and chisel to obtain 1–2 kg of material from weakly to moderately consolidated fault gouge. In order to define the cooling history of the country rock, we also collected three bedrock samples for low-temperature thermochronology at the Gediz detachment and three similar samples at the Büyük Menderes detachment. Note that although the three latter samples are included in a study on the exhumation of the Aydın Range (Nilius et al., 2019), they are also briefly described and presented in this study.

In the western part of the Gediz detachment, we sampled fault gouge at two recently created roadcuts (Fig. 1). At the first roadcut, sample 15T18 was collected from a low-angle normal fault, which dips gently to the north in the footwall of the Gediz detachment. The bedrock below and above the fault consists of phyllites and mylonitic quartzites of the Bayındır nappe (Fig. 2a). The fault zone exhibits a ~50-cm-thick layer of black to dark grey fault gouge and is cut by a steep north-dipping normal fault (85/70 N) (Fig. 2a and b). The sample for K-Ar dating was taken from the center of the fault gouge layer at a distance of several metres from the high-angle normal fault (Fig. 2c). About 3 km farther west, the Gediz detachment fault is well exposed in

another roadcut. Here, the detachment is characterised by a 10–15-cm-thick dark-grey fault gouge layer, which separates light grey marbles in the footwall from reddish sedimentary rocks in the hanging wall (Fig. 3a). The planar top of the detachment dips gently to the north (108/10 N) and exhibits a well-developed, NNW-plunging striation (337/08). The Neogene conglomerates in the hanging wall show numerous sheared and broken clasts (Fig. 3b). For K-Ar dating, sample 15T22 was collected from the lowermost 4 cm of the fault-gouge directly above the striated marbles (Fig. 3c). For low-temperature thermochronology, we took two bedrock samples from the footwall of the Gediz detachment (14M19 and 15M84) to the east and west of the two roadcuts, respectively (Fig. 1). A third bedrock sample (11M1) was taken a few kilometres farther north from a bedrock kippe in the hanging wall of the detachment.

At the Büyük Menderes detachment, the construction of a water reservoir offered the possibility to obtain fresh gouge material from the eastern portion of the fault (samples 15T2 and 15T3) (Fig. 1). The detachment separates deformed Neogene sedimentary rocks in the hanging wall from yellow quartzites in the footwall (Fig. 4a). The fault zone is 50–70 cm thick and became exposed over a distance of ~12 m during excavations related to dam construction. It dips gently to the SE (60/20 SE) and the planar schistosity of the fault gouge has striations with an orientation of 160/18. The fault zone consists of two gouge layers separated by a ~10-cm-thick zone of catactically deformed

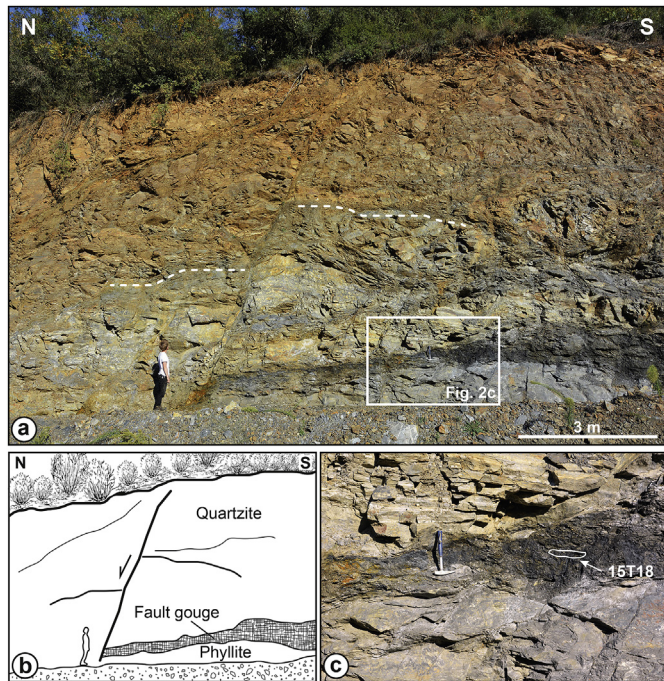


Fig. 2. Photographs of sampling site 15T18. **a)** Roadcut with the low-angle normal fault in the foreground from which sample 15T18 was obtained for K-Ar dating. Hanging wall of the fault consists of mylonitic quartzite, while the footwall comprises greyish phyllite. A steep normal fault cross-cuts and displaces the low-angle normal fault. Offset of bedrock is indicated by the white dashed line. **b)** Sketch of the outcrop shown in a). **c)** Sampled fault gouge horizon with hammer for scale. White outline corresponds to area from which sample 15T18 was obtained.

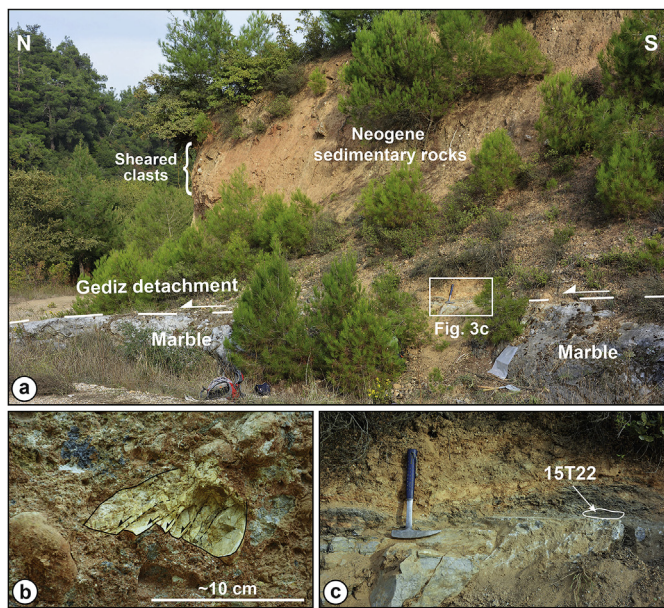


Fig. 3. Photographs of sampling site 15T22. **a)** Roadcut with Gediz detachment in the foreground. The hanging wall comprises deformed Neogene sedimentary rocks with numerous sheared clasts. The footwall of the detachment fault is marble. **b)** Sheared clast in Neogene sediments. Note that the sediment contains many brecciated rock fragments of different sizes. **c)** Sampled fault gouge horizon above the detachment fault surface. White outline corresponds to area from which sample 15T22 was obtained for K-Ar dating.

quartzite derived from the fault footwall. The upper gouge layer is rich in clay, light grey in colour and ~15 cm thick, whereas the dark grey gouge layer underneath contains less clay and has a thickness of ~30 cm. Samples for K-Ar dating were collected from the lower part of the light grey fault gouge (15T2) and from the lowermost 20 cm of the dark grey gouge layer (15T3) (Fig. 4b). As the water reservoir has been filled in the past years, the outcrop is no longer accessible.

About 7 km farther northeast, we obtained another fault gouge sample (16T6) from the Büyük Menderes detachment. This sampling site is located ~800 m higher than the outcrop at the water reservoir and the detachment forms a several hundred metres wide fault zone. The sample was collected from a > 5-m-thick zone with dark grey to black fault gouge near the crest of a NNE-trending mountain ridge (Fig. 5). The rocks above and below the fault gouge comprise weathered and sheared mica schists of the Bozdağ nappe. The sampled fault gouge layer is orientated subparallel to the foliation of the mica schists (i.e. 45/20 SE) (Fig. 5). We also obtained one sample (16M90) for low-temperature thermochronology from the mica schists (Nilius et al., 2019). South-dipping cataclasites about 400 m north of the sampling sites (Fig. 5) exhibit a top-to-the S sense of shear but are not suitable for K-Ar dating because they contain little clayey material. At the western part of the Büyük Menderes detachment we collected another fault gouge sample (15T7) in a small river valley that exposes > 5-m-thick cataastically deformed mylonites with a top-to-the S sense of shear (Fig. 1). The sample was collected from a ~0.5-m-thick fault zone, which dips south at an angle of 20–25° (i.e. slightly steeper than the foliation of the cataclasites). Striations on the main fault plane plunge towards the SSW. About 15 km east of this sampling site, we collected two samples for low-temperature thermochronology (15M57 and 15M58; Nilius et al., 2019) from the footwall of the detachment (Fig. 1).

4. K-Ar dating and hydrogen isotope analysis of fault gouges

4.1. Theoretical background

K-Ar dating of illite from fault gouges is increasingly applied to constrain the temporal activity of brittle faults (e.g. Vrolijk and van der Pluijm, 1999; Zwingmann and Mancktelow, 2004; Haines and van der Pluijm, 2008; Zwingmann et al., 2010; Duvall et al., 2011; Rahl et al., 2011; Haines et al., 2016; Mancktelow et al., 2016; Viola et al., 2016; Ring et al., 2017). Still, interpreting K-Ar ages for different clay size fractions from individual samples requires a careful examination of sample mineralogy, host rock lithology, and cooling histories to interpret the resulting bulk mineral ages in a meaningful way. For instance, protracted illite growth over a certain period of fault activity can be reflected by progressively younger ages for smaller size fractions, because larger crystals started to grow earlier than smaller ones (e.g. Zwingmann et al., 2010). On the other hand, K-Ar ages that increase with grain size may also result from contamination of the fault gouge with K-feldspar or muscovite from the host rock (e.g. van der Pluijm et al., 2001). In this case, older ages for larger size fractions may overestimate the time of faulting if significant amounts of K-feldspar or muscovite are present, whereas younger K-Ar ages for small size fractions without K-feldspar or inherited muscovite may record clay mineral growth during faulting (e.g. Haines and van der Pluijm, 2008; Hetzel et al., 2013; Viola et al., 2016). Knowledge of the cooling histories of crustal blocks adjacent to the studied fault can aid the evaluation of K-Ar fault gouge ages, because authigenic growth of illite during brittle faulting often occurs at temperature conditions bracketed by the annealing temperature of fission tracks in zircon (~240 °C) and the upper boundary of the partial annealing zones of apatite (~110 °C) (e.g. Zwingmann and Mancktelow, 2004; Mancktelow et al., 2016). This observation has been interpreted to indicate that K-Ar ages record illite growth during brittle faulting in this temperature interval. To determine the source of the water contained in the clay minerals of fault gouges, the hydrogen isotope analysis of muscovite and/or illite has

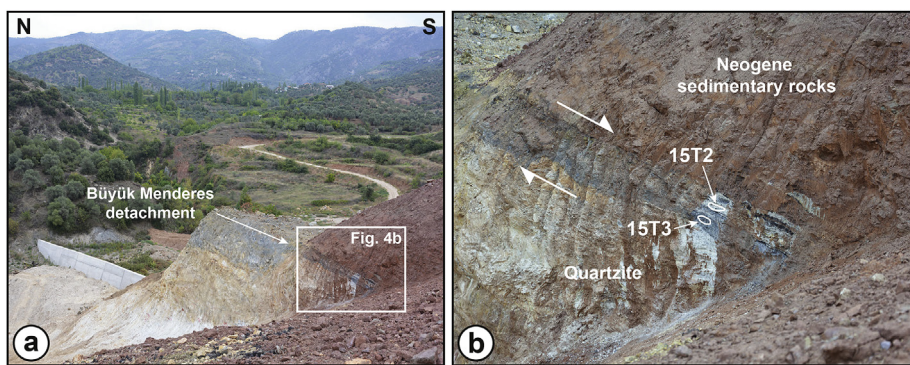


Fig. 4. Photographs of sampling site at the eastern Büyük Menderes detachment. **a)** The fault footwall consists of sheared quartzite, while the hanging wall comprises reddish Neogene sedimentary rocks. **b)** Close-up view with locations of K-Ar samples 15T2 and 15T3 indicated by white lines.

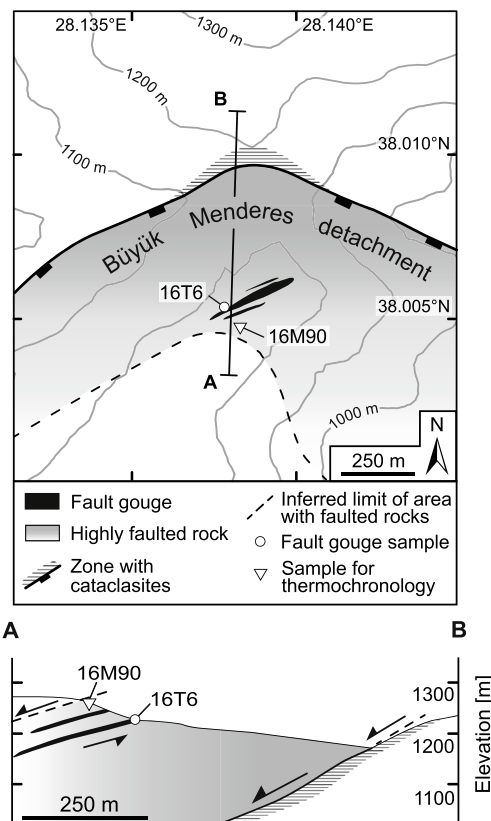


Fig. 5. Map and cross section of area at eastern end of the Büyük Menderes detachment fault where we took sample 16T6 for K-Ar dating and sample 16M90 for thermochronology. Rock deformation decreases in a southerly direction as indicated by the grey shading.

been particularly helpful (e.g. Fricke et al., 1992; Losh, 1997; Morrison and Anderson, 1998; Mulch et al., 2007; Mancktelow et al., 2016; Lynch et al., 2019).

4.2. K-Ar dating of fault gauges and results

The methodology used for K-Ar dating of the sampled fault gouges is similar to the one described by Zwingmann et al. (2010) and Hetzel et al. (2013). About 50–100 g of fresh fault gouge was gently disaggregated by repetitive freezing and thawing to avoid artificial grain-size reduction of rock components and contamination with K-bearing minerals such as K-feldspar and mica (Liewig et al., 1987). The grain-size fractions < 2 and 2–6 µm were separated in distilled water by gravity settling, whereas the fractions < 0.4 and < 0.1 µm were

separated with a high-speed centrifuge. The 2–6 µm size fraction was investigated to evaluate the influence of potential detrital contamination. The mineralogical composition of the fault gouge samples was determined by X-ray diffraction (XRD) (Table S1).

The K-Ar dating technique follows Dalrymple and Lanphere (1969) and Faure (1986). K-Ar isotopic determinations were performed following a procedure similar to that described by Bonhomme et al. (1975) and additional details can be found in Hetzel et al. (2013). For K analysis two sample aliquots of approximately 100 mg were required. Normally, 20 mg of sample material was required for Ar analysis. During the course of this study, two different age standards and three air shots were measured. The K-Ar dating results of samples and standards are summarised in Tables 1a and 1b. The error for Ar analyses is below 1% and the average $^{40}\text{Ar}/^{36}\text{Ar}$ value for the three air shots is 295.53 ± 0.27 (2σ) (Table 1c). Blanks for the extraction line and mass spectrometer were systematically determined and the mass discrimination factor was determined periodically by air shots. K-Ar ages were calculated using ^{40}K abundance and decay constants recommended by Steiger and Jäger (1977). The uncertainties of the K-Ar ages are given as 2σ and take into account the errors associated with sample weighing, $^{38}\text{Ar}/^{36}\text{Ar}$ and $^{40}\text{Ar}/^{38}\text{Ar}$ measurements, and K analysis.

The 19 K-Ar ages of the six fault gouge samples from the Büyük Menderes and Gediz normal fault systems range from ~22 to ~3 Ma (Table 1a). The K content ranges from a low 1.51% for sample 16T6 ($< 0.4 \mu\text{m}$) to 5.18% for sample 15T3 (combined < 0.1 and $< 0.4 \mu\text{m}$ size fractions) suggesting different mineralogy within the analysed clay fractions as confirmed by XRD results (Table S1). Radiogenic ^{40}Ar contents between 28% and 77% indicate good analytical conditions for all analyses except for the size fraction $< 0.1 \mu\text{m}$ of sample 15T22, which has a low radiogenic ^{40}Ar content of ~12% resulting in a larger error of the K-Ar age. At the Gediz detachment, K-Ar ages of 7–6 Ma were obtained from the three grain size fractions of sample 15T18, whereas sample 15T22 yielded three ages of ~12 Ma and one age of ~5 Ma for the smallest size fraction (Table 1a). The different grain size fractions of the samples 15T2 and 15T3 from the Büyük Menderes detachment have K-Ar ages of ~8.5 to ~2.8 Ma. In contrast, the size fractions of the fault gouge samples 15T7 and 16T6 from the Büyük Menderes detachment yielded older ages between ~22 and ~16 Ma (Table 1a).

4.3. Hydrogen isotope analysis of fault gouges and results

The hydrogen isotope (δD) values of six fault gouge samples were determined by continuous flow mass spectrometry using a high-temperature elemental analyser (Thermo Finnigan TC/EA) coupled to a mass spectrometer (Thermo Finnigan Delta V Advantage and 253) at the Goethe University – Senckenberg BiK-F Stable Isotope Facility Frankfurt. A sample weight of ca. 0.8 mg was wrapped into Ag foil and

Table 1a

K-Ar ages of fault gouges in the central Menderes Massif (Western Turkey).

Sample number ^a	Sample description	Latitude	Longitude	Grain size	K	Radiogenic ⁴⁰ Ar	Radiogenic ⁴⁰ Ar	Age	Error (2 σ)
		[°N]	[°E]	[μm]	[%]	[10 ⁻¹¹ mol/g]	[%]	[Ma]	[Ma]
<i>Gediz detachment – Bozdağ Range</i>									
15T18	dark grey fault gouge	38.4374	27.7969	< 0.1	3.73	4.035	29.5	6.2	0.2
15T18	"	"	"	< 2	4.53	5.551	28.3	7.1	0.3
15T18	"	"	"	2–6	4.53	5.818	42.3	7.4	0.2
15T22	dark grey fault gouge	38.4302	27.7691	< 0.1	2.78	2.259	11.8	4.7	0.9
15T22	"	"	"	< 0.4	3.04	6.061	27.9	11.5	0.3
15T22	"	"	"	< 2	2.92	6.111	33.1	12.0	0.4
15T22	"	"	"	2–6	2.30	4.624	33.2	11.6	0.8
<i>Büyük Menderes detachment – Aydin Range</i>									
15T2	light grey fault gouge	37.9612	28.0854	< 0.1	4.62	4.432	51.4	5.5	0.3
15T2	"	"	"	< 2	4.37	6.419	68.5	8.5	0.2
15T2	"	"	"	2–6	3.79	4.777	58.6	7.3	0.2
15T3	dark grey fault gouge	37.9612	28.0854	< 0.1 and < 0.4	5.18	2.543	39.8	2.8	0.2
15T3	"	"	"	< 2	4.28	4.663	68.1	6.3	0.2
15T3	"	"	"	2–6	2.96	3.325	71.9	6.5	0.2
15T7	black fault gouge	37.9359	27.6239	< 0.4	4.77	14.831	41.7	17.8	0.9
15T7	"	"	"	< 2	3.74	10.615	72.5	16.3	0.4
15T7	"	"	"	2–6	3.91	14.797	76.5	21.7	0.5
16T6	black fault gouge	38.0059	28.1389	< 0.4	1.51	4.972	51.8	18.9	0.6
16T6	"	"	"	< 2	1.98	6.358	66.6	18.4	0.5
16T6	"	"	"	2–6	1.65	5.518	72.2	19.2	0.5

dried overnight at 200 °C under vacuum in a stainless steel tray. Samples were rapidly transferred to a zero-blank autosampler in the stainless steel tray and the autosampler was immediately purged with helium gas to prevent rehydration of interlayer spacing or water adsorption on clay surfaces from ambient air moisture. Three internationally referenced standard materials and additional in-house working standards were run with the samples. After correction for mass bias, daily drift of the thermal combustion reactor, and offset from the certified reference values, NBS30 (biotite), NBS22 (oil), and CH7 (polyethylene foil) had δD values of −65‰, −118‰, and −103‰, respectively. Repeated measurements of the different standards and unknowns resulted in a precision of ± 3‰ for δD. All isotope ratios are reported relative to Vienna-Standard Mean Ocean Water (V-SMOW). The δD values of the fault gouge samples from the two fault systems fall in the range from −76 to −115‰ (Table 2).

5. Low-temperature thermochronology

5.1. Zircon and apatite fission-track analysis

For fission-track analysis, apatite and zircon grains were separated using conventional magnetic and heavy liquid separation techniques. Grains were embedded in PDA TeflonTM and epoxy, respectively, ground and polished. Apatites were etched with 5 M HNO₃ for 20 s at 21 °C (Donelick et al., 1999). Zircon mounts were etched in a KOH–NaOH eutectic melt at 215 °C (Zaun and Wagner, 1985). All samples

Table 1c
⁴⁰Ar/³⁶Ar values for airshots (n = 3).

Airshot-ID	⁴⁰Ar/³⁶Ar	Difference to reference value ^a
	[–]	[± %]
AS128-AirS-1	296.05	0.31
AS129-AirS-1	293.89	0.38
AS132-AirS-2	296.66	0.11

^a ⁴⁰Ar/³⁶Ar reference value of air from Steiger and Jäger (1977).

were irradiated with thermal neutrons at the FRM-II reactor facility in Garching (Technical University Munich, Germany). Fission-track counting was carried out with an Olympus BX-51 microscope under 1000 × magnification at the University Hannover. We applied the external detector method (Gleadow, 1981) with uranium-free muscovite sheets and the zeta calibration approach (e.g. Naeser, 1978; Hurford and Green, 1983) with dosimeter glass IRMM-540R and IRMM-541 and Durango apatite and Fish Canyon zircon age standards. To assess the annealing kinetics of apatite we measured D_{par} values (mean diameter of etch pits on prismatic surfaces of apatite parallel to the crystallographic c-axis) (Burtner et al., 1994). Zircon and apatite fission-track (ZFT and AFT) ages record cooling below a specific closure temperature, which varies within the partial annealing zone but is typically ~240 °C (zircon) and ~110 °C (apatite) (e.g. Gleadow and Duddy, 1981; Wagner and van den Haute, 1992). The fission track ages were

Table 1b

Age standards analysed (n = 6).

Standard ID	K	Radiogenic ⁴⁰ Ar	Radiogenic ⁴⁰ Ar	Age	Error (2 σ)	Difference to reference value ^a
	[%]	[10 ⁻¹⁰ mol/g]	[%]	[Ma]	[Ma]	[%]
HD-B1-132	7.96	3.404	91.27	24.50	0.38	+1.2
HD-B1-133	7.96	3.333	89.95	23.99	0.38	−0.91
HD-B1-138	7.96	3.442	93.22	24.77	0.32	+2.31
LP6-146	8.37	19.234	97.25	127.85	1.93	−0.04
LP6-147	8.37	19.292	96.78	128.22	1.92	+0.25
LP6-152	8.37	19.421	97.68	129.05	1.65	+0.90

^a Measured age standards include HD-B1 (Hess and Lippolt, 1994) and LP6 (Odin et al., 1982).

Table 2

Hydrogen isotope data of fault gouges from the central Menderes Massif.

Sample number	Weight [mg]	Grain size [μm]	δD^a [%]	K-Ar age [Ma]
<i>Bozdağ Range – Gediz detachment</i>				
15T18	0.817	< 0.1	-103	6.2 ± 0.2
15T18	0.809	< 2	-97	7.1 ± 0.3
15T18	0.874	2–6	-92	7.4 ± 0.2
15T22	0.861	< 0.1	-115	4.7 ± 0.9
15T22	0.903	< 0.4	-108	11.5 ± 0.3
15T22	0.900	< 2	-111	12.0 ± 0.4
15T22	0.881	2–6	-109	11.6 ± 0.8
<i>Aydın Range – Büyük Menderes detachment</i>				
15T2	0.255	< 0.1	-95	5.5 ± 0.3
15T2	0.811	< 2	-102	8.5 ± 0.2
15T2	0.841	2–6	-104	7.3 ± 0.2
15T3	0.855	< 0.1 and < 0.4	-106	2.8 ± 0.2
15T3	0.873	< 2	-102	6.3 ± 0.2
15T3	0.839	2–6	-97	6.5 ± 0.2
15T7	0.934	< 0.4	-76	17.8 ± 0.9
15T7	0.810	< 2	-87	16.3 ± 0.4
15T7	0.869*	2–6	-76*	21.7 ± 0.5
16T6	0.862*	< 0.4	-85*	18.9 ± 0.6
16T6	0.891	< 2	-90*	18.4 ± 0.5
16T6	0.846	2–6	-94	19.2 ± 0.5

^a Values marked with an asterisk are mean values from two sample aliquots.^b Ages as reported in Table 1a.calculated with the TRACKKEY software version 4.2 (Dunkl, 2002) and are reported with 2σ uncertainty (Table 3).

5.2. Zircon and apatite (U-Th)/He analysis

We employed (U-Th)/He dating on samples that yielded zircons and apatites of sufficient quality (Table 4). Zircon and apatite crystals were

hand-picked using a stereo and polarizing microscope under $200\times$ magnification following the selection criteria of Farley (2002) and Reiners (2005). Dimensions of the selected crystals were measured to determine alpha-ejection correction factors (Farley et al., 1996). Single crystals were loaded into pre-cleaned Pt tubes for He analysis, which was carried out at the Gööochron Laboratory (University of Göttingen, Germany). Extraction of helium from the crystals was performed by heating the encapsulated grains in vacuum with an IR laser. The extracted gas was purified by an SAES Ti-Zr getter and the He content was measured with a Hiden Hal-3F/PIC triple-filter quadrupole mass spectrometer. For measurements of the alpha-emitting elements U, Th, and Sm, the zircon and apatite crystals were dissolved and spiked with calibrated ^{233}U , ^{230}Th , and ^{149}Sm solutions. Zircons were dissolved in Teflon bombs with 48% HF and 65% HNO_3 at 220°C for five days, while apatites were dissolved in 2% ultrapure HNO_3 ($+0.05\%$ HF) in an ultrasonic bath. The actinide and Sm concentrations were measured by inductively coupled plasma mass spectrometry using the isotope dilution method. Measurements were carried out with a PerkinElmer Elan DRC II system equipped with an APEX micro-flow nebulizer. Errors for the single-grain zircon and apatite (U-Th)/He ages include the uncertainties of the He, U, Th, and Sm measurements and the estimated uncertainty of the ejection correction factor. Zircon and apatite (U-Th)/He (= ZHe and AHe) ages are interpreted to record the cooling below the closure temperatures of $\sim 180^\circ\text{C}$ (zircon) and $\sim 70^\circ\text{C}$ (apatite), respectively, although the exact closure temperature can vary within the partial retention zone (e.g. Wolf et al., 1998; Farley, 2000; Reiners et al., 2004). Reported ZHe and AHe ages are the unweighted mean of the single-grain ages of each sample given with 2 standard errors (Table 4).

5.3. Results from low-temperature thermochronology

The two samples from the footwall of the western Gediz detachment

Table 3

Results of apatite and zircon fission track analysis.

Sample ^a	Latitude	Longitude	Elevation	Number of crystals	ρ_s^b	N_s^b	ρ_i^b	N_i^b	ρ_d^b	N_d^b	P (χ^2) ^b	Disper-sion	Central age $\pm 2\sigma$	U	D _{par}
[°N]	[°E]	[m]												[ppm]	[μm]
Apatite fission track (AFT)															
<i>Footwall of Gediz detachment (Bozdağ Range)</i>															
14M19	38.4324	27.8355	556	20	0.720	29	13.325	537	8.3596	3032	39	0.35	5.7 ± 2.6	22	1.30
15M84	38.4309	27.7362	244	16	1.373	35	8.824	225	4.6428	2796	99	0	8.2 ± 3.2	31	2.74
<i>Hanging wall of Gediz detachment (Bozdağ Range)</i>															
11M1	38.4805	27.8105	190	20	0.885	17	18.490	355	17.087	4424	100	0	10.4 ± 2.8	15	1.48
<i>Footwall of Büyük Menderes detachment (Aydın Range)</i>															
14M35*	37.9537	28.1034	766	11	0.788	7	15.444	139	8.1684	3032	50	0	5.2 ± 4.0*	27	1.55
14M41*	37.9682	28.0899	406	11	0.847	16	18.201	344	8.0970	3032	29	0	4.4 ± 2.2	33	1.54
15M57 ^s	37.9684	27.7614	705	8	1.383	13	7.234	68	5.1285	2796	99	0	10.6 ± 6.6	20	2.00
15M58 ^s	37.9574	27.7586	292	22	1.546	45	21.306	620	5.1076	2796	80	0	4.3 ± 1.4	58	2.34
16M90 ^s	38.0048	28.1380	1255	35	3.929	163	23.769	986	6.8920	2481	99	0	12.9 ± 2.6	48	1.68
<i>Hanging wall of Büyük Menderes detachment (Aydın Range)</i>															
14M31*	37.9227	28.0861	829	15	2.887	41	17.042	242	8.2282	3032	50	0	17.8 ± 6.2*	31	1.73
Zircon fission track (ZFT)															
<i>Footwall of Gediz detachment (Bozdağ Range)</i>															
14M19	see above		8		17.755	87	67.347	330	6.821	2583	69	0	9.8 ± 2.4	508	–
15M84	"		25		9.877	100	33.778	342	6.308	1982	99	0	14.1 ± 3.6	228	–
<i>Hanging wall of Gediz detachment (Bozdağ Range)</i>															
11M1	see above		20		90	531	100.678	594	6.525	2512	2	0.24	32.8 ± 5.8	634	–
<i>Footwall of Büyük Menderes detachment (Aydın Range)</i>															
15M57 ^s	"		20		19.172	147	42.213	316	6.419	1982	20	0.20	19.1 ± 4.8	224	–
<i>Hanging wall of Büyük Menderes detachment (Aydın Range)</i>															
14M31*	see above		20		75.225	835	96.757	1074	6.814	2583	8	0.13	29.0 ± 3.8	585	–

^a Samples marked with an asterisk are from Wölfler et al. (2017). Samples included in Nilius et al. (2019) are marked with a section sign (\$).^b The density of spontaneous and induced tracks (ρ_s and ρ_i) is given in units of 10^5 tracks/cm². N_s and N_i correspond to the number of counted spontaneous and induced tracks, respectively. N_d is the number of counted tracks on the dosimeter. The probability of obtaining a chi-square value (χ^2) for n degrees of freedom (where n is the number of crystals minus 1) is indicated as P (χ^2).

Table 4
Results of zircon and apatite (U-Th)/He geochronology.

Sample ^a	Aliq.	He	238U			232Th			Th/U ratio			Sm			Ejection correction ^b			Uncorrected age ± 2σ ^c	Ft-corrected age ± 2σ ^c	Sample age ± 2 s.e. ^d
			Vol. [10 ⁻⁹ cm ³]	1σ [%]	Mass [ng]	1σ Conc. [%]	Mass [ng]	1σ Conc. [%]	Mass		1σ	Conc.	Mass		1σ	Conc.				
									[ng]	[ng]	[%]	[%]	[ng]	[%]	[%]	[%]	[Ma]	[Ma]	[Ma]	
Zircon (U/Th)/He																				
Footwall of Gediz detachment (Bozdağ Range)	14M19 #1	395.965	1.1	3.962	1.8	346	1.454	2.4	127	0.37	0.114	5.3	10	0.84	715.04	851.2 ± 53.0*	14.6 ± 1.9			
	#2	2.790	1.2	1.785	1.8	156	0.814	2.4	71	0.46	0.027	9.4	2	0.83	11.68	14.07 ± 0.91				
	#3	1.584	1.2	0.977	1.8	338	0.888	2.4	307	0.91	0.018	9.7	6	0.73	11.04	15.13 ± 1.36				
	#4	0.503	1.7	1.680	1.8	461	0.430	2.4	118	0.26	0.025	10.6	7	0.74	2.34	3.16 ± 0.29*				
Hanging wall of Gediz detachment (Bozdağ Range)	11M1 #1	4.682	1.7	2.222	1.8	444	0.452	2.4	9.0	0.20	0.025	12.8	5	0.78	16.64	21.39 ± 1.75	23.4 ± 1.3			
	#2	1.863	1.8	0.743	1.8	148	0.589	2.4	14	0.79	0.015	14.5	4	0.76	17.46	22.90 ± 1.95				
	#3	2.380	1.8	0.986	1.8	197	0.210	2.4	7.1	0.21	0.005	24.3	2	0.73	19.01	25.92 ± 2.42				
Footwall of Büyükk Menderes detachment (Aydin Range)	14M35* #1	1.398	0.9	0.944	1.8	248	0.849	2.4	223	0.90	0.241	9.6	63	0.77	10.09	13.10 ± 1.01	15.7 ± 3.6			
	#2	3.577	0.9	1.806	1.8	340	1.261	2.4	238	0.70	0.216	9.6	41	0.77	14.06	18.26 ± 1.41				
	#3	1.636	0.9	0.753	1.8	604	0.260	2.4	208	0.34	0.025	11.3	20	0.64	16.61	26.0 ± 3.0*				
	#4	3.125	1.2	2.314	1.8	286	0.613	2.4	76	0.27	0.006	16.4	1	0.81	10.50	12.99 ± 0.91	12.2 ± 0.7			
Footwall of Büyükk Menderes detachment (Aydin Range)	14M35* #1	0.909	1.3	0.810	1.8	258	0.228	2.4	73	0.28	0.003	25.8	1	0.73	8.70	11.93 ± 1.09				
	#2	1.773	0.9	1.576	1.8	422	0.484	2.4	129	0.31	0.035	10.5	9	0.74	8.70	11.74 ± 1.02				
	#3	4.611	1.3	3.151	1.8	591	0.502	2.4	94	0.16	0.302	15.7	6	0.78	11.67	14.99 ± 1.18	14.2 ± 0.4			
	#2	5.701	1.3	3.664	1.8	832	0.273	2.4	62	0.07	0.210	15.7	5	0.94	12.66	13.47 ± 0.63				
Footwall of Büyükk Menderes detachment (Aydin Range)	#3	6.538	1.3	4.883	1.8	1291	0.528	2.4	140	0.11	0.406	15.7	11	0.76	10.81	14.15 ± 1.17				
	#1	4.466	1.3	3.068	1.8	93	1.271	2.4	38	0.41	0.994	15.7	3	0.86	10.95	12.78 ± 0.76	13.3 ± 0.5			
	#2	11.496	1.3	8.473	1.8	476	1.118	2.4	63	0.13	0.408	15.7	2	0.84	10.89	12.90 ± 0.82				
	#3	9.012	1.3	5.666	1.8	351	2.050	2.4	127	0.36	0.740	15.7	5	0.85	12.12	14.25 ± 0.87				
Hanging wall of Büyükk Menderes detachment (Aydin Range)	16M90 [§] #2	4.474	1.1	2.487	1.8	462	1.600	2.4	297	0.64	0.027	9.5	5	0.75	12.93	17.28 ± 1.46	18.9 ± 2.2			
	#3	3.637	1.0	2.044	1.8	406	0.130	2.4	25	0.06	0.009	15.8	2	0.71	14.52	20.45 ± 1.96				
	#1	1.476	1.2	0.812	1.8	231	0.180	2.4	51	0.22	0.013	10.2	4	0.76	14.30	18.80 ± 1.56				
Apatite (U/Th)/He	14M31* #1	8.919	1.1	4.403	1.8	737	0.580	2.4	97	0.13	0.108	5.0	18	0.77	16.30	21.11 ± 1.69	20.0 ± 1.6			
	#2	8.919	1.1	4.403	1.8	737	0.580	2.4	97	0.13	0.108	5.0	18	0.77						
Hanging wall of Gediz detachment (Bozdağ Range)																				
Footwall of Gediz detachment (Bozdağ Range)	11M1 #1	0.0004	76.5	0.001	102.4	0.4	0.005	5.3	1.6	3.51	0.031	36.7	10	0.70	1.08	1.6 (+2.8/-1.6)	3.2 ± 2.3			
	#2	0.001	57.2	0.001	208.4	0.3	0.004	5.8	1.6	5.51	0.009	34.8	4	0.70	3.42	4.9 (+9.8/-4.9)				
	#3	0.008	6.3	0.011	5.2	6.7	0.007	3.7	4.3	0.64	0.076	9.1	48	0.65	5.14	7.90 ± 1.45*	3.0 ± 0.3			
	#2	0.027	3.6	0.081	1.9	12	0.056	2.6	8.0	0.69	0.318	6.5	46	0.77	2.29	2.98 ± 0.31				
Hanging wall of Büyükk Menderes detachment (Aydin Range)	14M31* #1	0.131	1.5	0.615	1.8	57	0.277	2.4	25	0.45	0.650	6.2	60	0.81	1.58	1.95 ± 0.14	1.6 ± 0.2			
	#2	0.163	1.5	1.190	1.8	79	0.036	2.7	2.4	0.03	0.720	6.0	48	0.80	1.12	1.40 ± 0.11				
	#3	0.171	1.4	1.190	1.8	79	0.058	2.6	3.9	0.05	0.771	6.0	51	0.80	1.17	1.46 ± 0.11				
	#1	0.001	11.0	0.003	16.7	1.7	0.004	4.0	2.3	1.35	0.095	8.2	52	0.70	2.28	3.26 ± 1.03	3.3 ± 1.0			

^a Samples marked with an asterisk are from Wölfli et al. (2017). Samples included in Nilius et al. (2019) are marked with a section sign (§).

^b Ejection correction (Ft): correction factor for alpha-ejection (according to Farley et al., 1996 and Hourigan et al., 2005).

^c Uncertainty of the single-grain ages includes both the analytical uncertainty and the estimated uncertainty of the ejection correction. Ft-corrected (U-Th)/He ages marked with asterisk are not considered in the calculation of the sample age.

^d Sample age is the unweighted average age of all Ft-corrected (U-Th)/He ages (± 2 standard error).

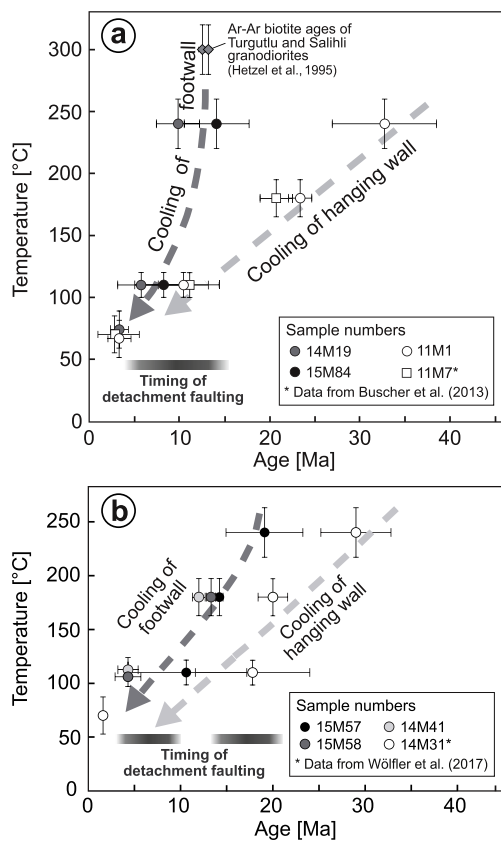


Fig. 6. Cooling paths for the footwall and hanging wall of the a) Gediz and b) Büyükk Menderes detachments based on thermochronologic data (Tables 3 and 4). We also plotted ^{40}Ar - ^{39}Ar biotite ages for the Turgutlu and Salihli granodiorites (Hetzell et al., 1995) and the ZHe, AFT, and AHe ages for sample 11M7 (an orthogneiss klippe on the Gediz detachment; Buscher et al., 2013). In plot b) we also show the ZFT, ZHe, AFT, and AHe ages of sample 14M31 (an orthogneiss klippe above the Büyükk Menderes detachment; Wölfle et al., 2017). The activity of both detachments – based on the interpretation of K-Ar ages and thermochronology data from this work and previously published studies – is shown in the lower part of both plots.

(15M84 and 14M19; Fig. 1) yielded zircon fission track (ZFT) ages of 14.1 ± 3.6 Ma and 9.8 ± 2.4 Ma and apatite fission track (AFT) ages of 8.2 ± 3.2 and 5.7 ± 2.6 Ma, respectively (Table 3). Sample 14M19 gave an AHe age of 3.3 ± 1.0 Ma (Table 4). Taken together these ages indicate relatively rapid cooling (~ 240 – ~ 70 °C) of the footwall rocks between ~ 14 and ~ 3 Ma (Fig. 6a). In contrast, the thermochronologic ages for sample 11M1 suggest that the hanging wall cooled slowly since the Oligocene (ZFT age: 32.8 ± 5.8 Ma; ZHe age: 23.4 ± 1.3 Ma; AFT age: 10.4 ± 2.8 Ma; AHe age: 3.2 ± 2.3 Ma).

The two footwall samples from the western Büyükk Menderes detachment (15M57 and 15M58; Fig. 1), yielded ZHe ages of 14.2 ± 0.4 and 13.3 ± 0.5 Ma, respectively, whereas sample 16M90 from the eastern end of the detachment gave a slightly older age of 18.9 ± 2.2 Ma (Table 4). The AFT ages of these three samples range from 12.9 ± 2.6 to 4.3 ± 1.4 Ma; a ZFT age was only obtained for sample 15M57 (i.e. 19.1 ± 4.8 Ma) (Table 3). Taken together, the ages record the cooling of the footwall of the Büyükk Menderes detachment since ~ 20 Ma (Fig. 6b). The hanging wall of the detachment cooled more slowly as constrained by sample 14M31 from Wölfle et al. (2017) (Fig. 6b). The combination of apatites with low uranium content and young cooling ages resulted in small numbers of horizontally confined fission tracks. Therefore, mean track lengths for the AFT dataset cannot be reported. However, published AFT track lengths for samples from the footwall of the Gediz and Büyükk Menderes detachments range from 14.1 to 14.2 μm and from 13.0 to 13.3 μm , respectively, indicating quite

rapid cooling (Ring et al., 2003; Wölfle et al., 2017).

6. Discussion

6.1. Interpretation of the K-Ar and thermochronologic data

We combine our results from K-Ar dating and low-temperature thermochronology to evaluate the timing of brittle faulting on the Gediz and Büyükk Menderes detachment faults. The ages from both data sets are summarised in Fig. 7 together with previously published age data (Lips et al., 2001; Buscher et al., 2013; Hetzell et al., 2013; Wölfle et al., 2017).

At the Gediz detachment, sample 15T22 from the fault gouge layer between marble in the footwall and Neogene sediments in the hanging wall (Fig. 3a) yielded within error identical K-Ar ages of 11.6 ± 0.8 , 12.0 ± 0.4 , and 11.5 ± 0.3 Ma for three size fractions, whereas the smallest fraction gave a younger age of 4.7 ± 0.9 Ma (Table 1a). Sheared clasts in the sedimentary rocks document brittle deformation and cataclasis of these rocks during their tectonic emplacement on the detachment surface (Fig. 3b). This synextensional deformation explains the presence of quartz in the two coarse grained size fractions of sample 15T22 (25% and 6%) and traces of K-feldspar in the 2–6 and $< 2 \mu\text{m}$ size fractions (3% and $< 1\%$; Table S1), which cannot be derived from the marble unit in the fault footwall. The presence of detrital quartz and K-feldspar raises the question if the K-Ar ages are affected by inherited muscovite from the sedimentary rocks (cf. van der Pluijm et al., 2001; Bense et al., 2014; Viola et al., 2018). In that case, the ages of 12–11 Ma would only provide an upper limit for the age of gouge formation and faulting. As no data on the mineralogical composition of the Neogene sediments are available, it is not possible to exclude this possibility, even though our field observations did not reveal any muscovite in the sediments. Notably, sample 15T22 only contains the 2M1 illite polytype and is devoid of 1M illite (Table S1), which is often considered to be derived from the transformation of the high-temperature 2M1 polytype or from muscovite (e.g. Haines and van der Pluijm, 2012). For the following reasons, we consider the presence of significant amounts of inherited muscovite in sample 15T22 as unlikely. Firstly, fission track dating of detrital apatite in the lower part of the Neogene sedimentary succession revealed different age components between ~ 15 and ~ 30 Ma (Asti et al., 2018). Thus, apatite has not been reset in the sedimentary rocks but records cooling of the host rock. This implies that potentially present muscovite in the Neogene sediments cannot have been reset either and must be even older than 15–30 Ma due to its higher closure temperature compared to apatite. If detrital muscovite grains were present in the fault-gouge sample, a larger scatter in the K-Ar ages would be expected (cf. van der Pluijm et al., 2001; Torgersen et al., 2015), in particular because the illite content of the fault gouge varies from 17% in the 2–6 μm fraction to 51% in the $< 0.4 \mu\text{m}$ fraction (Table S1). For these reasons, we interpret the K-Ar ages of 12–11 Ma to record the growth of authigenic 2M1 illite during an early stage of detachment faulting and gouge formation. This interpretation is consistent with ZFT and AFT ages of 14.1 ± 3.6 and 8.2 ± 3.2 Ma for sample 15M84 (Table 3, Fig. 7), which indicate that cooling from ~ 240 °C to ~ 110 °C occurred during normal faulting at the Gediz detachment in this time interval (Fig. 6a). The youngest K-Ar age of 4.7 ± 0.9 Ma may date the growth of fine-grained ($< 0.1 \mu\text{m}$) illite near the end of detachment faulting (as further discussed below).

Fault gouge sample 15T18 was collected 3 km farther east, from a low-angle normal fault in the footwall of the Gediz detachment (Fig. 2). The three grain size fractions of this sample yielded K-Ar ages that decrease from 7.4 ± 0.2 to 6.2 ± 0.2 Ma with decreasing grain size (Table 1a). As for sample 15T22, there are two possible interpretations of the age data. The two slightly older ages of 7.4 ± 0.2 and 7.1 ± 0.3 Ma may simply reflect that illite growth in the 2–6 and $< 2 \mu\text{m}$ size fractions started earlier than in the smaller $< 0.1 \mu\text{m}$ fraction (cf. Zwingmann et al., 2010). This interpretation is supported by ZFT

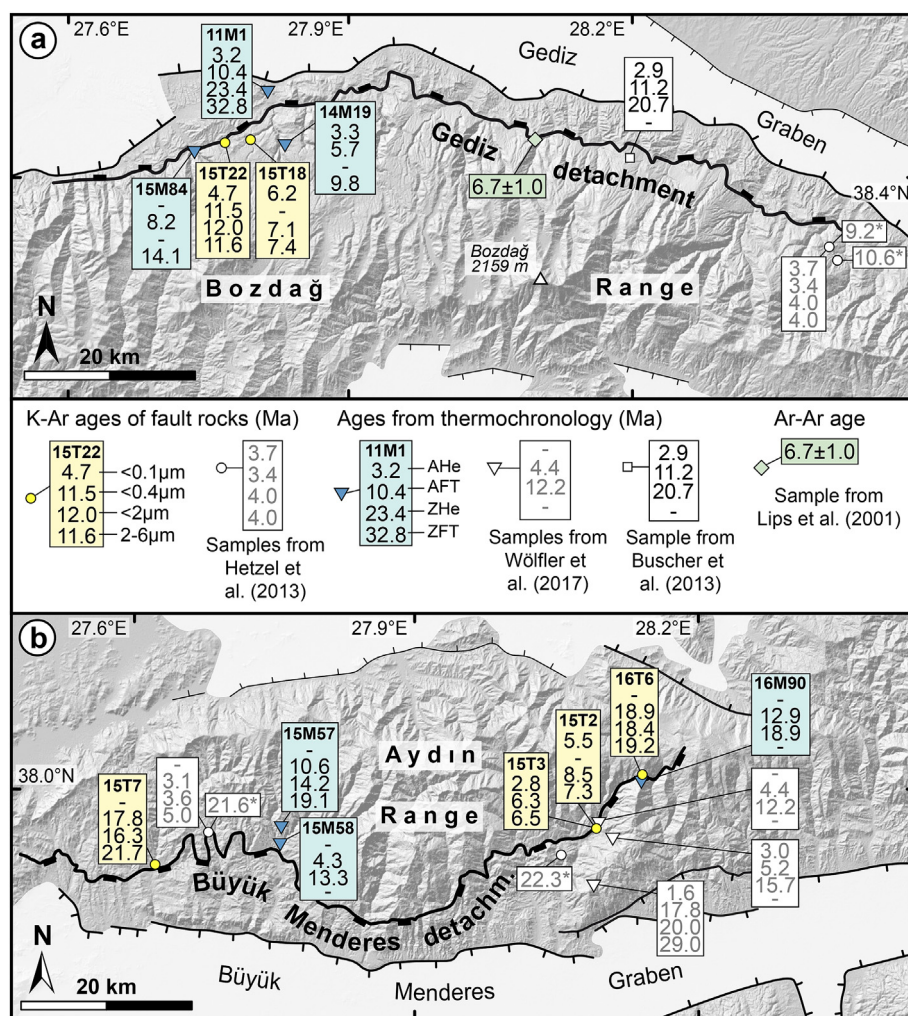


Fig. 7. Shaded relief map of the a) Bozdağ and b) Aydin ranges with K–Ar ages of fault gouges and ages from low-temperature thermochronology. K–Ar ages are indicated for different grain size fractions. K–Ar ages marked with an asterisk have been determined for the < 2 µm fraction. In the Bozdağ Range cooling ages from an orthogneiss klippe above the Gediz detachment (Buscher et al., 2013) and an ^{40}Ar - ^{39}Ar age from synkinematic white mica from the footwall of the Gediz detachment (Lips et al., 2001) are also indicated.

and AFT ages of 9.8 ± 2.4 and 5.7 ± 2.6 Ma for the nearby sample 14M19, which record a significant cooling of the fault footwall (Figs. 6a and 7) at the time recorded by the K–Ar ages (i.e. 7–6 Ma). Alternatively, the observed relation between age and grain size may be caused by inherited muscovite from the mylonitic quartzites and phyllites that constitute the host rock of the fault (Fig. 2a). The mean ^{40}Ar - ^{39}Ar fusion age of 6.7 ± 1.0 Ma obtained for white mica from a mylonitic quartzite at the Gediz detachment (Lips et al., 2001) may support this second interpretation, although we note that the respective sample is from an outcrop ~30 km farther to the east (Fig. 7). In our opinion, the first interpretation is more likely for two reasons. Firstly, ongoing normal faulting at 7–6 Ma can readily explain the Late Miocene cooling indicated by the thermochronological data. Secondly, a short-lived marine transgression into the supradetachment basin above the Gediz detachment, which occurred in the upper Tortonian (8.35–7.25 Ma; MMi 12 biozone), records increased subsidence by normal faulting (Asti et al., 2019) and coincides with the two K–Ar ages for the larger grain-size fractions.

As discussed above, the fault gouge samples from the western Gediz detachment (15T18 and 15T22) contain only the 2M1 illite polytype. Since the illite content in the smallest size fraction of both samples (i.e. < 0.1 µm) is lower than the one in the < 0.4 and < 2 µm fractions (Table S1), the young K–Ar ages of 6.2 ± 0.2 and 4.7 ± 0.9 Ma for the smallest fractions (Table 1a) may record the latest illite growth during

faulting. Apart from illite, the samples contain relatively large amounts of smectite (28–68%; Table S1), a clay mineral that is only stable at temperatures below ~ 100 –80 °C (Pytte and Reynolds, 1989; Huang et al., 1993). Thus, we infer that the growth of smectite occurred during a late stage of normal faulting when temperatures had fallen below ~ 100 –80 °C (cf. Viola et al., 2016). Two similar AHe ages of 3.3 ± 1.0 and 3.2 ± 2.3 Ma for bedrock samples from the footwall and hanging wall of the western Gediz detachment indicate cooling to ~ 70 °C (14M19 and 11M1; Fig. 1) and suggest that the activity of the detachment system came to an end before ~ 3 Ma (Fig. 6a). Hence, the K–Ar ages of 6.2 ± 0.2 Ma (sample 15T18) and 4.7 ± 0.9 Ma (15T22) may reflect the last increment of faulting at the western Gediz detachment system.

At the eastern Büyük Menderes detachment, sample 16T6 was collected from a thick fault gouge layer within the broad fault zone (Fig. 5). The three grain size fractions analysed from this sample yielded within error identical and consistent K–Ar ages of 19.2 ± 0.5 , 18.4 ± 0.5 , and 18.9 ± 0.6 Ma (Table 1a, Fig. 7). All size fractions contain significant amounts of 1M illite (13–21%) and mixed layer illite-smectite (18–32%), but only minor 2M1 illite (6–8%; Table S1), indicating gouge formation and clay mineral growth at temperatures slightly above the partial annealing zone of apatite (cf. Zwingmann et al., 2010). This inference is broadly consistent with a ZHe age of 18.9 ± 2.2 Ma and an AFT age of 12.9 ± 2.6 Ma for sample 16M90

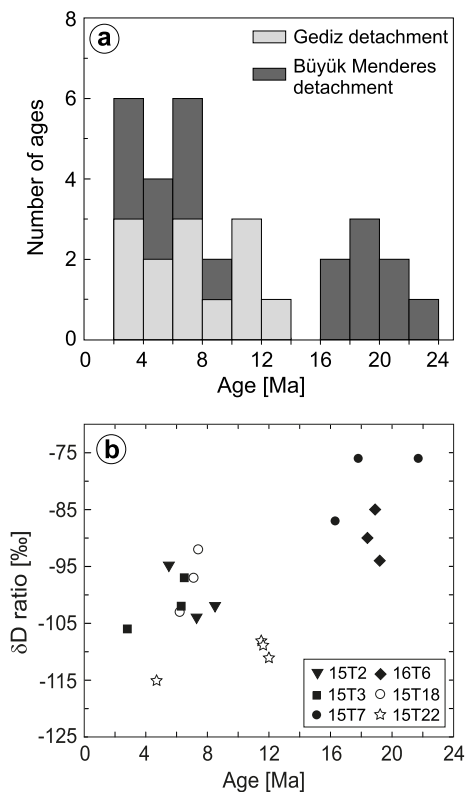


Fig. 8. a) K-Ar ages of fault gouge and cataclasite samples in the central Menderes Massif (data from this study and from Hetzel et al., 2013). The ages of all grain size fractions have been plotted. b) K-Ar ages of fault gouge samples (all grain size fractions) plotted versus δD isotope ratios. Samples from the Büyük Menderes and Gediz detachment faults are indicated with closed and open symbols, respectively.

(Tables 3 and 4, Fig. 7), which bracket the time when the fault rocks were at temperatures between ~ 180 and ~ 110 °C. Minor traces of K-feldspar (2–4%) in the 2–6 and $< 2\text{ }\mu\text{m}$ size fractions have no recognisable effect on the K-Ar ages, probably because the small feldspar grains were isotopically reequilibrated due to fluid-rock interaction (cf. Zwingmann et al., 2010). We thus interpret the K-Ar ages to reflect illite growth during detachment faulting at 19–18 Ma.

Markedly younger K-Ar ages were determined for the two fault gouge samples 15T2 and 15T3 from the outcrop at the Büyük Menderes detachment that was excavated for construction of a water reservoir (Figs. 4 and 7). The two samples contain 7–15% 2M1 illite, 4–13% 1M illite (except the $< 0.1\text{ }\mu\text{m}$ fraction of sample 15T2, which is devoid of the latter), and 36–81% illite/smectite (Table S1). Apart from the temperature decrease during normal faulting and progressive exhumation, the presence of different illite types may be explained by changes in the composition of externally-derived fluids (see discussion below). The six K-Ar ages from the two samples range from 8.5 ± 0.2 to 2.8 ± 0.2 Ma (Table 1a, Fig. 7). Although it is not possible to exclude the presence of inherited muscovite from the host rock of the detachment (i.e., quartzite in the footwall and sedimentary rocks in the hanging wall; Fig. 4), a systematic decrease of the K-Ar ages with grain size – as commonly observed in such cases (Viola et al., 2013; Torgersen et al., 2015) – does not occur in the samples (Table 1a). In sample 15T2, the oldest age of 8.5 ± 0.2 Ma was obtained for the intermediate size fraction, whereas in sample 15T3 two similar ages of ~ 6.5 and ~ 6.3 Ma for the larger fractions are about twice as old as the youngest age of ~ 2.8 Ma (Fig. 7). We therefore interpret the K-Ar ages to reflect prolonged illite growth during detachment faulting between ~ 9 and 3 Ma. This interpretation is consistent with a phase of late Miocene to Pliocene footwall cooling constrained by ZHe ages of 15.7 ± 3.6 and

12.2 ± 0.7 Ma and AFT ages of 5.2 ± 4.0 and 4.4 ± 2.2 Ma (samples 14M35 and 14M41; Tables 3 and 4, Fig. 7; Wölfle et al., 2017). An alternative interpretation would be that the two samples are affected by inherited muscovite from the host rock of the detachment. In this case, the older ages of ~ 8 –6 Ma would overestimate the age of faulting, while the youngest ages in both samples (5.5 ± 0.3 and 2.8 ± 0.2 Ma) may record illite growth during brittle deformation. This interpretation would agree with published K-Ar fault gouge ages of ~ 5 –3 Ma for a sample in the western part of the detachment fault (Fig. 7, sample 09Me-NM01; Hetzel et al., 2013). In any case, we interpret the high amounts of illite/smectite in samples 15T2 and 15T3 – in addition to the other illite polytypes – to be related to the infiltration of the Büyük Menderes detachment by K-rich fluids. The occurrence of illite/smectite in this detachment is in contrast to the Gediz detachment, where illite/smectite is completely lacking. These observations support the notion that – apart from temperature – host-rock mineralogy and fluid chemistry are important factors controlling the types of authigenic clay minerals in low-angle normal faults (Haines and van der Pluijm, 2012).

The fault gouge sample from the western Büyük Menderes detachment (15T7) yielded similar but more variable K-Ar ages than sample 16T6 from the eastern part of the fault. The fault gouge contains large quantities of the 2M1 illite polytype (45–58%) but is devoid of 1M illite (Table S1). The three ages of 21.7 ± 0.5 , 16.3 ± 0.4 , and 17.8 ± 0.9 Ma (Table 1a) neither correlate with the amount of 2M1 illite nor with the grain size of the analysed fractions. Given that the sampled fault developed within cataastically deformed mylonites, initial faulting possibly occurred at temperatures close to the ductile-brittle transition, which would be in agreement with the growth of authigenic 2M1 illite (e.g. Haines and van der Pluijm, 2008; Ring et al., 2017). The interpretation that faulting began at rather high temperature is supported by the ZFT age of 19.1 ± 4.8 Ma of sample 15M57, which indicates initial cooling from ductile conditions to below ~ 240 °C at about ~ 19 Ma (Table 3). Together with the ZHe age of 14.2 ± 0.4 Ma for the same sample (Table 4), the thermochronological data suggest that cooling from ~ 240 °C to ~ 180 °C occurred between ~ 19 and ~ 14 Ma (Fig. 6b). Hence, we interpret the K-Ar ages to reflect an early phase of detachment faulting between ~ 22 and ~ 16 Ma, which is also recorded in the eastern part of the detachment by K-Ar ages of ~ 19 –18 Ma for sample 16T6. This interpretation is consistent with a previously published K-Ar age of 21.6 ± 0.6 Ma for a nearby cataclasite sample from the Büyük Menderes detachment (sample 09Me-NM02; Hetzel et al., 2013) (Fig. 7). Minor amounts of smectite present in samples 15T7 and 16T6 may have grown at lower temperature (cf. Viola et al., 2016), either during the second phase of deformation or after brittle faulting had ceased.

Hydrogen isotope ratios of the analysed fault gouges range from -76 to -115‰ (Table 2, Fig. 8b) and indicate interaction with infiltrating meteoric water during gouge formation and faulting (e.g. Fricke et al., 1992; Losh, 1997; Morrison and Anderson, 1998; Mulch et al., 2007). Similar δD values of -89 to -95‰ were recently reported for two fault gouges samples from the Naxos detachment, possibly indicating a similar isotopic composition of the precipitation source for this core complex in the late Miocene (Mancktelow et al., 2016). Interestingly, the fault gouges from the Büyük Menderes detachment with early Miocene K-Ar ages exhibit δD values between -76 and -94‰ , whereas those of the younger fault gouges are more negative, with values between -92 and -115‰ (Fig. 8b). To evaluate whether this difference is related to changes in paleo-elevation during the formation of the Menderes metamorphic core complex is beyond the scope of the present study. The pattern is, however, consistent with a) meteoric fluid interaction at increasingly shallower levels of the extending crust and interaction with less-evolved meteoric fluids, and b) with an increase in elevation of the Menderes metamorphic core complex over time. The latter is supported by the recent finding of an upper Tortonian (~ 8 Ma) limestone horizon in the clastic sedimentary succession of the Gediz supradetachment basin (Asti et al., 2019). From the

current elevation of the outcrop (~ 760 m) and an estimated water depth of 100 ± 50 m below sea level during limestone deposition, Asti et al. (2019) calculated a rock uplift of 860 ± 50 m.

6.2. Detachment faulting and exhumation of the central Menderes Massif

The timing of normal faulting at the Gediz and Büyükk Menderes detachment systems and the question whether faulting was continuous or episodic through time has been much debated (e.g. Gessner et al., 2001; Ring et al., 2003; Purvis and Robertson, 2005; Öner and Dilek, 2011; Buscher et al., 2013; Rossetti et al., 2017; Wölfle et al., 2017). We now use our K-Ar ages together with previously published geochronological data (Fig. 7) to summarise the history of normal faulting and rock exhumation at both detachment faults.

In the western portion of the Gediz detachment, our oldest K-Ar ages, which we interpret to indicate faulting at 12–11 Ma (sample 15T22), are similar to two K-Ar ages of ~ 10.6 and ~ 9.2 Ma for fault gouges from the eastern part of the detachment system (Fig. 7; Hetzel et al., 2013). Taken together, these ages indicate that brittle faulting was underway along the entire detachment at that time. Detachment faulting during the middle Miocene is also indicated by ^{40}Ar - ^{39}Ar biotite ages of 13.1 ± 0.2 and 12.2 ± 0.4 Ma for the synextensional Turgutlu and Salihli granodiorites (Hetzel et al., 1995), and by slightly older U-(Th)-Pb ages of ~ 15 –14 Ma for titanite from the Salihli granodiorite (Rossetti et al., 2017). Our younger K-Ar ages of 7–6 Ma for sample 15M18 from a normal fault in the footwall of the western Gediz detachment are remarkably similar to an ^{40}Ar - ^{39}Ar age of 6.7 ± 1.0 Ma for synkinematic white mica from a mylonite sample beneath the central part of the detachment (Fig. 7; Lips et al., 2001). These ages indicate ongoing normal faulting during the late Miocene. The K-Ar age of 4.7 ± 0.9 Ma (sample 15T22) may record the last increment of deformation in the western part of the detachment, whereas still younger K-Ar fault gouge ages of 4–3 Ma suggest that faulting continued until ~ 3 Ma ago in the easternmost part of the Gediz detachment system (Hetzel et al., 2013) (Fig. 7). Together with the cooling history of the footwall and hanging wall (Fig. 6a), the presently available age data suggest that the Gediz detachment fault was active rather continuously between ~ 15 and ~ 3 Ma, although faulting in the western part appears to have ceased 1–2 Ma earlier. A phase of particularly fast cooling and exhumation between ~ 4 and ~ 2 Ma has only been reported for the eastern Gediz detachment (Salihli area) (Buscher et al., 2013) and was confirmed by Plio-Quaternary cooling ages from detrital apatite fission track analysis (Asti et al., 2018). The pronounced late Pliocene activity of the eastern Gediz detachment in the Salihli region is in agreement with the remarkable preservation of the fault in that area, where the detachment exerts a dominant control on the current topography.

In contrast to the Gediz detachment, K-Ar ages of fault gouge samples from the Büyükk Menderes detachment system form two distinct groups (Fig. 8a), suggesting that the detachment was active during two phases. Our K-Ar ages of two fault gouge samples from the eastern and western part of the Büyükk Menderes detachment, together with two published K-Ar ages (Hetzel et al., 2013) and cooling ages from low-temperature thermochronology (Figs. 6b and 7), suggest that the first phase of normal faulting occurred at ~ 22 –16 Ma along the entire detachment. The thermochronologic data of Wölfle et al. (2017) and Nilius et al. (2019) indicate that cooling and rock exhumation during this phase continued into the middle Miocene, although this has not yet been recorded by fault-gouge dating. The second phase of normal faulting occurred between ~ 9 and ~ 3 Ma, as indicated by our new and previously published K-Ar fault gouge ages (Figs. 7 and 8a). This second stage of faulting is corroborated by low-temperature thermochronologic data in the eastern part of the detachment, which document a phase of enhanced footwall cooling in the latest Miocene and Pliocene (Wölfle et al., 2017).

6.3. Implications for the development of metamorphic core complexes

Our combined data set of K-Ar and thermochronological ages provides constraints on the evolution of the central Menderes Massif, which is among the few bivariant metamorphic core complexes worldwide. Other examples of bivariant core complexes include the Shuswap core complex in Canada (Vanderhaeghe et al., 1999, 2003) and the Wugongshan dome in China (Faure et al., 1996). Most core complexes are, however, asymmetric and controlled by only one detachment fault (e.g. Crittenden et al., 1980; Lister and Davis, 1989; Malavieille et al., 1993; Whitney et al., 2013). This also applies to the Aegean region, where extension is primarily accommodated by single detachment faults (e.g. Jolivet et al., 2010, 2015), with bivariant extension being mostly restricted to the islands of the western Cyclades (Grasemann et al., 2012).

Numerical models indicate that the formation of bivariant metamorphic core complexes requires high intra-crustal strength contrasts and a weak lower crust (e.g. Gessner et al., 2007; Huet et al., 2011; Labrousse et al., 2016; Wu and Lavier, 2016). Other factors that promote the development of bivariant core complexes include crustal layering and dipping lithological contrasts inherited from the orogenic shortening phase, as well as changes in the thermal state and strain rates (Huet et al., 2011; Labrousse et al., 2016; Wu and Lavier, 2016). For the central Menderes Massif, this may imply that strength contrasts inherited from Early Tertiary nappe stacking and the formation of a tear in the subducting Aegean slab with the related rise of hot asthenosphere (Biryol et al., 2011; Prelević et al., 2012, 2015; Jolivet et al., 2015), have aided the development of the bivariant core complex. As a result of core-complex formation and ongoing extension, the central Menderes Massif is characterized by high surface heat flow, high geothermal gradients, and widespread geothermal activity (Ilkişik, 1995; Dolmaz et al., 2005; Gessner et al., 2018).

In general, geochronological constraints on the duration of detachment faulting indicate time periods of 5–25 Ma (e.g. Foster and John, 1999; Vanderhaeghe et al., 2003; Brichau et al., 2008; Colgan et al., 2010; Campani et al., 2010; Whitney et al., 2013; Singleton et al., 2014). Our data show that this also applies to the pair of detachments bounding the central Menderes Massif. The Gediz detachment was active from ~ 15 to ~ 3 Ma, whereas the Büyükk Menderes detachment experienced two phases of faulting between ~ 22 and ~ 3 Ma (Figs. 6 and 8a). Whether such a diachronous formation of two detachment faults with opposite dips and sense of shear is typical for the evolution of bivariant core complexes is, however, difficult to decide due to the limited availability of geochronological data that accurately constrain the time of faulting in other bivariant core complexes (cf. Grasemann et al., 2012). At least in the Shuswap complex, the onset of bivariant extension appears to have occurred at similar times on both sides of the complex (Vanderhaeghe et al., 2003). From numerical experiments, it may be expected that the development of detachment pairs may not be synchronous, in particular if lateral gradients in crustal strength and temperature exist (cf. Labrousse et al., 2016; Wu and Lavier, 2016).

After the onset of bivariant extension, the two detachments may operate at similar rates, as indicated by slip rates derived from low-temperature thermochronology in the central Menderes Massif. For the Gediz detachment, ZHe ages along a profile parallel to the tectonic transport direction yield a slip rate of $4.3^{+3.0}_{-1.2}$ km/Ma (Buscher et al., 2013), whereas the Büyükk Menderes detachment system was active at a rate of 2.6 ± 2.1 km/Ma in the Pliocene (Nilius et al., 2019). In this context, we note that the high slip rate of ~ 12.5 km/Ma, which Oner Baran et al. (2017) derived from their own ZHe ages along the same profile at the Gediz detachment as Buscher et al. (2013), results from an error in the applied distance between the samples (cf. Oner Baran et al., 2017, compare their Figs. 3 and 4a). A re-evaluation of their data with corrected distances between their ZHe samples yields a slip rate of 4.6 ± 2.8 km/Ma, which agrees with the rate of Buscher et al. (2013). A comparison with a compilation of slip rates for

detachment faults worldwide (Webber et al., 2018) shows that the slip rates of the Gediz and Büyükk detachment represent moderate values within the reported range of 1–15 km/Ma. Finally, thermochronological data reveal that slip accumulation on low-angle detachment faults is associated with considerable footwall cooling, which implies that these structures provide an efficient mechanism for rock exhumation from mid-crustal levels (e.g. Foster and John, 1999; Brichau et al., 2008; Singleton et al., 2014).

7. Conclusions

In this study, we employed K-Ar dating of fault gouges and low-temperature thermochronology to constrain the timing of detachment faulting at the Gediz and Büyükk Menderes detachments in the central Menderes Massif (Western Turkey). The new K-Ar ages reveal that the western Gediz detachment was active from ~12 to ~5 Ma, with a late Pliocene phase of faulting being only recorded in the eastern part of the detachment fault. Previously published age data indicate that detachment faulting and rapid cooling of the footwall rocks started already at ~15 Ma. In contrast to the Gediz detachment, the Büyükk Menderes detachment was active during two phases of faulting. As indicated by our new and previously published K-Ar ages, the first phase lasted from ~22 to 16 Ma, although thermochronologic data suggest that footwall cooling and rock exhumation continued during the middle Miocene. A second phase of detachment faulting occurred in the late Miocene and Pliocene and lasted from ~9 to 3 Ma. During this time span, both detachments were active simultaneously and caused the bivariant exhumation of the central Menderes core complex. The youngest K-Ar ages and cooling histories for hanging and footwall rocks imply that the activity of both detachments ended ~3 Ma ago. Hydrogen isotope ratios of -76 to -115‰ for fault gouges from both detachments indicate interaction with infiltrating meteoric fluids during detachment faulting and gouge formation.

Acknowledgements

This study was funded by the Deutsche Forschungsgemeinschaft (DFG) grants HE 1704/18-1 and GL 724/7-1 provided to R. Hetzel and C. Glotzbach, and by the Leibniz Universität Hannover (start-up funds to A. Hampel). We thank Cris Lana and Espen Torgersen for their insightful reviews, which significantly improved the original version of the manuscript.

Appendix A. Supplementary data

Supplementary data to this article can be found online at <https://doi.org/10.1016/j.jsg.2019.103865>.

References

- Mulch, A., Teyssier, C., Cosca, M.A., Chamberlain, C.P., 2007. Stable isotope paleoaltimetry of Eocene core complexes in the North American Cordillera. *Tectonics* 26 (4). <https://doi.org/10.1029/2006TC001995>. TC4001.
- Asti, R., Malusà, M.G., Faccenna, C., 2018. Supradetachment basin evolution unravelled by detrital apatite fission track analysis: the Gediz Graben (Menderes Massif, Western Turkey). *Basin Res.* 30 (3), 502–521.
- Asti, R., Faccenna, C., Rossetti, F., Malusà, M.G., Gliozzi, E., Faranda, C., Lirer, F., Cosentino, D., 2019. The Gediz supradetachment system (SW Turkey): magmatism, tectonics, and sedimentation during crustal extension. *Tectonics* 38, 1414–1440.
- Ault, A.K., Reiners, P.W., Evans, J.P., Thomson, S.N., 2015. Linking hematite (U-The)/He dating with the microtextural record of seismicity in the Wasatch fault damage zone, Utah, USA. *Geology* 43 (9), 771–774.
- Bense, F.A., Wemmer, K., Löbens, S., Siegesmund, S., 2014. Fault gouge analyses: K-Ar illite dating, clay mineralogy and tectonic significance—a study from the Sierras Pampeanas, Argentina. *Int. J. Earth Sci.* 103, 189–218.
- Biryol, B.C., Beck, S.L., Zandt, G., Özcar, A.A., 2011. Segmented African lithosphere beneath the Anatolian region inferred from teleseismic P-wave tomography. *Geophys. J. Int.* 184, 1037–1057.
- Bonhomme, M.G., Thuijzer, R., Pinault, Y., Clauer, N., Wendling, R., Winkler, R., 1975. Méthode de Datation Potassium-Argon. Appareillage et Technique, Strasbourg.
- Braun, J., van der Beek, P., Valla, P., Robert, X., Herman, F., Glotzbach, C., Pedersen, V., Perry, C., Simon-Labrec, T., Prigent, C., 2012. Quantifying rates of landscape evolution and tectonic processes by thermochronology and numerical modeling of crustal heat transport using PECUBE. *Tectonophysics* 524, 1–28.
- Brichau, S., Ring, U., Carter, A., Bolhar, R., Monié, P., Stockli, D., Brunel, M., 2008. Timing, slip rate, displacement and cooling history of the Mykonos detachment footwall, Cyclades, Greece, and implications for the opening of the Aegean Sea basin. *J. Geol. Soc.* 165, 263–277 London.
- Brun, J.-P., Sokoutis, D., 2010. 45 m.y. of Aegean crust and mantle flow driven by trench retreat. *Geology* 38 (9), 815–818.
- Burchfiel, B.C., Chen, Z., Hodges, K.V., Yuping, L., Royden, L.H., Changrong, D., Jiene, X., 1992. The South Tibetan Detachment System, Himalayan Orogen: Extension Contemporaneous with and Parallel to Shortening in a Collisional Mountain Belt. vol. 269. Geological Society of America, pp. 1–41 Special Paper.
- Burtner, R., Nigrini, A., Donelick, R.A., 1994. Thermochronology of lower cretaceous source rocks in the Idaho-Wyoming thrust belt. *American Assoc. Petrol. Geol. Bulletin* 78, 1613–1636.
- Buscher, J.T., Hampel, A., Hetzel, R., Dunkl, I., Glotzbach, C., Struffert, A., Akal, C., Rätz, M., 2013. Quantifying rates of detachment faulting and erosion in the central Menderes Massif (western Turkey) by thermochronology and cosmogenic ¹⁰Be. *J. Geol. Soc. London* 170 (4), 669–683.
- Caine, J.S., Evans, C.B., Forster, J.P., 1996. Fault zone architecture and permeability structure. *Geology* 24 (11), 1025–1028.
- Campani, M., Herman, F., Mancktelow, N., 2010. Two- and three-dimensional thermal modeling of a low-angle detachment: exhumation history of the Simplic Fault Zone, central Alps. *J. Geophys. Res.* 115, B10420. <https://doi.org/10.1029/2009JB007036>.
- Candan, O., Dora, O.Ö., Oberhänsli, R., Çetinkaplan, M., Partzsch, J.H., Warkus, F.C., Dürr, S., 2001. Pan-african high-pressure metamorphism in the precambrian basement of the Menderes massif, western anatolia, Turkey. *Int. J. Earth Sci.* 89, 793–811.
- Candan, O., Oberhänsli, R., Dora, O.Ö., Çetinkaplan, M., Korale, E., Rimmelé, G., Chen, F., Akal, C., 2011. Polymetamorphic evolution of the pan-african basement and palaeozoic-early tertiary cover series of the Menderes massif. *Bulletin of the Mineral Research and Exploration* 142, 121–163.
- Catlos, E.J., Çemen, I., 2005. Monazite ages and the evolution of the Menderes Massif, western Turkey. *Int. J. Earth Sci.* 94, 204–217.
- Choo, C.O., Chang, T.W., 2000. Characteristics of clay minerals in gouges of the Dongrae fault, Southeastern Korea, and implications for fault activity. *Clay Clay Miner.* 48 (2), 204–212.
- Colgan, J.P., Howard, K.A., Fleck, R.J., Wooden, J.L., 2010. Rapid middle Miocene extension and unroofing of the southern Ruby Mountains, Nevada. *Tectonics* 29, TC6022. <https://doi.org/10.1029/2009TC002655>.
- Crittenden, M.D., Coney, P.J., Davis, G.H., 1980. Cordilleran Metamorphic Core Complexes, vol. 153. Geological Society of America, Memoir, pp. 490.
- Dalrymple, G.B., Lanphere, M.A., 1969. Potassium-Argon Dating: Principles, Techniques and Applications to Geochronology. W.H. Freeman, San Francisco.
- Dewey, J.F., 1988. Extensional collapse of orogens. *Tectonics* 7 (6), 1123–1139.
- Dolmaz, M.N., Hisarli, Z.M., Ustaömer, T., Orbay, N., 2005. Curie point depths based on spectrum analysis of aeromagnetic data, West Anatolian extensional province, Turkey. *Pure Appl. Geophys.* 162, 571–590.
- Donelick, R.A., Ketcham, R.A., Carlson, W.D., 1999. Variability of apatite fission track annealing kinetics II: crystallographic orientation effects. *Am. Mineral.* 84, 1224–1234.
- Dora, O.Ö., Kun, N., Candan, O., 1990. Metamorphic history and geotectonic evolution of the Menderes massif. *Proceedings of International Earth Sciences Congress on Aegean Region, Izmir/Turkey*, vol. 2. pp. 102–115.
- Dunkl, I., 2002. TRAKKEY: a Windows program for calculation and graphical presentation of fission track data. *Comput. Geosci.* 28 (1), 3–12.
- Duvall, A.R., Clark, M.K., van der Pluijm, B.A., Li, C., 2011. Direct dating of Eocene reverse faulting in northeastern Tibet using Ar-dating of fault clays and low-temperature thermochronometry. *Earth Planet. Sci. Lett.* 304 (3–4), 520–526.
- Eide, E.A., Torsvik, T.H., Andersen, T.B., 1997. Absolute dating of brittle fault movements: late Permian and late Jurassic extensional fault breccias in western Norway. *Terra. Nova* 9, 135–139.
- Emre, T., 1996. The tectonic evolution of the Gediz graben. *Geol. Bull. Turk.* 39, 1–18.
- Farley, K.A., 2000. Helium diffusion from apatite: general behavior as illustrated by Durango fluorapatite. *J. Geophys. Res.* 105 (B2), 2903–2914.
- Farley, K.A., 2002. U-Th/He dating: techniques, calibrations and applications. *Rev. Mineral. Geochem.* 47, 819–844.
- Farley, K.A., Wolf, R.A., Silver, L.T., 1996. The effects of long alpha-stopping distances on (U-Th)/He ages. *Geochim. Cosmochim. Acta* 60, 4223–4229.
- Faure, G., 1986. Principles of Isotope Geology. John Wiley and Sons, New York.
- Faure, M., Sun, Y., Shu, L., Monié, P., Charvet, J., 1996. Extensional tectonics within a subduction-type orogen. The case study of the Wugongshan dome (Jiangxi Province, southeastern China). *Tectonophysics* 263 (1–4), 77–106.
- Forsyth, D.W., 1992. Finite extension and low-angle normal faulting. *Geology* 20 (1), 27–30.
- Foster, D.A., John, B.E., 1999. Quantifying tectonic exhumation in an extensional orogen with thermochronology: examples from the southern Basin and Range Province. In: In: Ring, U., Brandon, M.T., Lister, G.S., Willett, S.D. (Eds.), Exhumation Processes: Normal Faulting, Ductile Flow, and Erosion, vol. 154. Geological Society of London, Special Publications, pp. 343–364.
- Fricke, H.C., Wickham, S.M., O'Neil, J.R., 1992. Oxygen and hydrogen isotope evidence for meteoric water infiltration during mylonitization and uplift in the Ruby Mountains-East Humboldt Range core complex, Nevada. *Contrib. Mineral. Petro.* 111 (2), 203–221.
- Gébelin, A., Teyssier, C., Heizler, M., Mulch, A., 2015. Meteoric water circulation in a

- rolling-hinge detachment system (northern Snake Range core complex, Nevada). Geological Society of America. Bulletin 127 (1–2), 149–161.
- Gessner, K., Ring, U., Johnson, C., Hetzel, R., Passchier, C.W., Güngör, T., 2001. An active bivergent rolling-hinge detachment system: central Menderes metamorphic core complex in western Turkey. *Geology* 29 (7), 611–614.
- Gessner, K., Wijns, C., Moresi, L., 2007. Significance of strain localization in the lower crust for structural evolution and thermal history of metamorphic core complexes. *Tectonics* 26, TC2012. <https://doi.org/10.1029/2004TC001768>.
- Gessner, K., Gallardo, L.A., Markwitz, V., Ring, U., Thomson, S.N., 2013. What caused the denudation of the Menderes Massif: review of crustal evolution, lithosphere structure, and dynamic topography on southwest Turkey. *Gondwana Res.* 24 (1), 243–274.
- Gessner, K., Markwitz, V., Güngör, T., 2018. Crustal fluid flow in hot continental extension: tectonic framework of geothermal areas and mineral deposits in western Anatolia. In: Gessner, K., Blenkinsop, T.G., Sorjonen-Ward, P. (Eds.), *Characterization of Ore-Forming Systems from Geological, Geochemical and Geophysical Studies*, vol. 453. Geological Society of London, Special Publications, pp. 289–311.
- Gleadow, A.J.W., 1981. Fission-track dating methods: what are the real alternatives? *Nucl. Tracks* 5, 3–14.
- Gleadow, A.J.W., Duddy, I.R., 1981. A natural long-term track annealing experiment for apatite. *Nucl. Tracks* 5 (1–2), 169–174.
- Glodny, J., Hetzel, R., 2007. Precise U–Pb ages of syn-extensional Miocene intrusions in the central Menderes Massif, western Turkey. *Geol. Mag.* 144 (2), 235–246.
- Grasemann, B., Schneider, D.A., Stöckli, D.F., Iglseder, C., 2012. Miocene bivergent crustal extension in the Aegean: evidence from the western Cyclades (Greece). *Lithosphere* 4, 23–39.
- Gürer, Ö.F., Sarica-Filoreau, N., Özburan, M., Sangu, E., Doğan, B., 2009. Progressive development of the Büyük Menderes Graben based on new data, western Turkey. *Geol. Mag.* 146 (5), 652–673.
- Haines, S.H., van der Pluijm, B.A., 2008. Clay quantification and Ar–Ar dating of synthetic and natural gouge: application to the Miocene Sierra Mazatán detachment fault, Sonora, Mexico. *J. Struct. Geol.* 30 (4), 525–538.
- Haines, S.H., van der Pluijm, B.A., 2012. Patterns of mineral transformations in clay gouge, with examples from low-angle normal fault rocks in the western USA. *J. Struct. Geol.* 43, 2–32.
- Haines, S.H., Lynch, E., Mulch, A., Valley, J.W., van der Pluijm, B., 2016. Meteoric fluid infiltration in crustal-scale normal fault systems as indicated by $\delta^{18}\text{O}$ and $\delta^2\text{H}$ geochemistry, and $^{40}\text{Ar}/^{39}\text{Ar}$ dating of neoformed clays in brittle fault rocks. *Lithosphere* 8 (6), 587–600.
- Hess, J.C., Lippolt, H.J., 1994. Compilation of K/Ar measurements on HD-B1 standard biotite; 1994 status report. In: Odin, G.S. (Ed.), *Phanerozoic Time Scale*. Bulletin de Liaison et d'information. IUGS Subcommission, Geochronology, Paris, pp. 19–23.
- Hetzel, R., Reischmann, T., 1996. Intrusion age of Pan-African augen gneisses in the southern Menderes Massif and the age of cooling after Alpine ductile extensional deformation. *Geol. Mag.* 133 (5), 565–572.
- Hetzel, R., Ring, U., Akal, C., Troesch, M., 1995. Miocene NNE-directed extensional unroofing in the Menderes Massif, southwestern Turkey. *J. Geol. Soc. London* 152 (4), 639–654.
- Hetzel, R., Romer, R.L., Candan, O., Passchier, C.W., 1998. Geology of the Bozdağı area, central Menderes massif, SW Turkey: pan-african basement and alpine deformation. *Int. J. Earth Sci.* 87 (3), 394–406.
- Hetzel, R., Zwingmann, H., Mulch, A., Gessner, K., Akal, C., Hampel, A., Güngör, T., Petschick, R., Mikes, T., Wedin, F., 2013. Spatiotemporal evolution of brittle normal faulting and fluid infiltration in detachment fault systems: a case study from the Menderes Massif, western Turkey. *Tectonics* 32, 1–13.
- Hourigan, J.K., Reiners, P.W., Brandon, M.T., 2005. U-Th zonation-dependent alpha-ejection in (U-Th)/He chronometry. *Geochim. Cosmochim. Acta* 69, 3349–3365.
- Huang, W.L., Longo, J.M., Pevear, D.R., 1993. An experimentally derived kinetic model for smectite-to-illite conversion and its use as a geothermometer. *Clay Clay Miner.* 41, 162–177.
- Huet, B., Le Pourhiet, L., Labrousse, L., Burov, E., Jolivet, L., 2011. Post-orogenic extension and metamorphic core complexes in a heterogeneous crust: the role of crustal layering inherited from collision. Application to the Cyclades (Aegean domain). *Geophys. J. Int.* 184, 611–625.
- Hurford, A.J., Green, P.F., 1983. The zeta age calibration of fission-track dating. *Chem. Geol.* 1, 285–317.
- Ilkişik, O.M., 1995. Regional heat flow in western Anatolia using silica temperature estimates from thermal springs. *Tectonophysics* 244, 175–184.
- İşk, V., Seyitoğlu, G., Çemen, I., 2003. Ductile-brittle transition along the Alaşehir detachment fault and its structural relationship with the Simav detachment fault, Menderes massif, western Turkey. *Tectonophysics* 374 (1), 1–18.
- Jolivet, L., Faccenna, C., 2000. Mediterranean extension and the Africa-Eurasia collision. *Tectonics* 19 (6), 1095–1106.
- Jolivet, L., Lecomte, E., Huet, B., Denèle, Y., Lacombe, O., Labrousse, L., Le Pourhiet, L., Mehl, C., 2010. The north cycladic detachment system. *Earth Planet. Sci. Lett.* 289, 87–104.
- Jolivet, L., Faccenna, C., Huet, B., Labrousse, L., Le Pourhiet, L., Lacombe, O., Lecomte, E., Burov, E., Denèle, Y., Brun, J.P., et al., 2013. Aegean tectonics: strain localization, slab tearing and trench retreat. *Tectonophysics* 597, 1–33.
- Jolivet, L., Menant, A., Sternai, P., Rabillard, A., Arbaret, L., Augier, R., Laurent, V., Beaudoin, A., Grasemann, B., Huet, B., Labrousse, L., Le Pourhiet, L., 2015. The geological signature of a slab tear below the Aegean. *Tectonophysics* 659, 166–182.
- Kralik, M., Klima, K., Riedmüller, G., 1987. Dating fault gouges. *Nature* 327, 315–317.
- Labrousse, L., Huet, B., Le Pourhiet, L., Jolivet, L., Burov, E., 2016. Rheological implications of extensional detachments: mediterranean and numerical insights. *Earth Sci. Rev.* 161, 233–258.
- Liewig, N., Clauer, N., Sommer, F., 1987. Rb-Sr and K-Ar dating of clay diagenesis in Jurassic sandstone oil reservoirs, North Sea. *American Assoc. Petrol. Geol. Bulletin* 71, 1467–1474.
- Lips, A.L.W., Cassard, D., Sözbilir, H., Yilmaz, H., Wijbrans, J.R., 2001. Multistage exhumation of the Menderes massif, western Anatolia (Turkey). *Int. J. Earth Sci.* 89, 781–792.
- Lister, G.S., Davis, G.A., 1989. The origin of metamorphic core complexes and detachment faults formed during Tertiary continental extension in the northern Colorado River region. *U.S.A.J. Struc. Geol.* 11 (1–2), 65–94.
- Losh, S., 1997. Stable isotope and modelling studies of fluid-rock interaction associated with the Snake Range and Mormon Peak detachment faults, Nevada. *Geological Society of America. Bulletin* 109 (3), 300–323.
- Lynch, E.A., Mulch, A., Yonkee, A., van der Pluijm, B., 2019. Hydrogen isotopes in authigenic clay minerals suggest presence of surface fluids in the evolving Sevier fold-thrust belt of ID-WY. *Earth Planet. Sci. Lett.* 513, 29–39.
- Lyons, J.B., Snellenburg, J., 1971. Dating faults. *Geological society of America. Bulletin* 82 (6), 1749–1752.
- Malavieille, J., 1993. Late orogenic extension in mountain belts: insights from the Basin and Range and the Late Paleozoic Variscan belt. *Tectonics* 12 (5), 1115–1130.
- Mancktelow, N., Zwingmann, H., Mulch, A., 2016. Dating of fault gouge from the Naxos detachment (Cyclades, Greece). *Tectonics* 35 (10), 2334–2344.
- McCallister, A.T., Taylor, M.H., Murphy, M.A., Styron, R.H., Stockli, D.F., 2014. Thermochronologic constraints on the late Cenozoic exhumation history of the Gurla Mandhata metamorphic core complex, Southwestern Tibet. *Tectonics* 33, 27–52.
- McKenzie, D., 1978. Active tectonics of the Alpine-Himalayan belt: the Aegean Sea and surrounding regions. *Geophys. J. Int.* 55 (1), 217–254.
- Morrison, J., Anderson, J.L., 1998. Footwall refrigeration along a detachment fault: implications for the thermal evolution of core complexes. *Science* 279 (5347), 63–66.
- Mulch, A., Chamberlain, C.P., 2007. Stable isotope paleoaltimetry in orogenic belts – the silicate record in surface and crustal geological archives. *Rev. Mineral. Geochem.* 66 (1), 89–118.
- Naeser, C.W., 1978. Fission track dating. *U.S. Geol. Survey. Open. File. Rep.* 76–190.
- Nilius, N.-P., Glotzbach, C., Wölfle, A., Hampel, A., Dunkl, I., Akal, C., Heineke, C., Hetzel, R., 2019. Exhumation History of the Aydin Range and Role of the Büyük Menderes Detachment System during Bivergent Extension of the Central Menderes Massif, Western Turkey. *Journal of the Geological Society, London*. <https://doi.org/10.1144/jgs2018-162>.
- Odin, G.S., collaborators, 1982. Interlaboratory standards for dating purposes. In: Odin, G.S. (Ed.), *Numerical Dating in Stratigraphy*, Part 1. John Wiley and Sons, Chichester, pp. 123–148.
- Öner, Z., Dilek, Y., 2011. Supradetachment basin evolution during continental extension: the Aegean province of western Anatolia, Turkey. *Geological Society of America. Bulletin* 123 (11–12), 2115–2141.
- Oner Baran, Z., Dilek, Y., Stockli, D., 2017. Diachronous uplift and cooling history of the Menderes core complex, western Anatolia (Turkey), based on new Zircon (U-Th)/He ages. *Tectonophysics* 694, 181–196.
- Özer, S., Sözbilir, H., 2003. Presence and tectonic significance of Cretaceous rudist species in the so-called Permo-Carboniferous Göktepe Formation, central Menderes metamorphic massif, western Turkey. *Int. J. Earth Sci.* 92 (3), 397–404.
- Prelević, D., Akal, C., Foley, S.F., Romer, R.L., Stracke, A., van den Bogaard, P., 2012. Ultratopassic mafic rocks as geochemical proxies for post-collisional dynamics of orogenic lithospheric mantle: the case of southwestern Anatolia, Turkey. *J. Petrol.* 53, 1019–1055.
- Prelević, D., Akal, C., Romer, R.L., Mertz-Kraus, R., Helvacı, C., 2015. Magmatic response to slab tearing: constraints from the ayyon alkaline volcanic complex, western Turkey. *J. Petrol.* 56, 527–562.
- Purvis, M., Robertson, A., 2005. Sedimentation of the Neogene-Recent Alaşehir (Gediz) continental graben system used to test alternative tectonic models for western (Aegean) Turkey. *Sediment. Geol.* 173 (1–4), 373–408.
- Pytte, A.M., Reynolds, R.C., 1989. The thermal transformation of smectite to illite. In: Naeser, N.D., McCulloch, T.H. (Eds.), *Thermal History of Sedimentary Basins*. Springer, New York, pp. 133–140.
- Rahl, J.M., Haines, S.H., van der Pluijm, B.A., 2011. Links between orogenic wedge deformation and erosional exhumation: evidence from illite age analysis of fault rock and detrital thermochronology of syn-tectonic conglomerates in the Spanish Pyrenees. *Earth Planet. Sci. Lett.* 307 (1–2), 180–190.
- Reiners, P.W., 2005. Zircon (U-Th)/He thermochronometry. *Rev. Mineral. Geochem.* 58, 151–179.
- Reiners, P.W., Spell, T.I., Nicolescu, S., Zanetti, K., 2004. Zircon (U-Th)/He thermochronometry: He diffusion and comparisons with $^{40}\text{Ar}/^{39}\text{Ar}$ dating. *Geochem. Cosmochim. Acta* 68 (8), 1857–1887.
- Ring, U., Brandon, M.T., Lister, G.S., Willett, S.D., 1999. Exhumation processes. In: Ring, U., Brandon, M.T., Lister, G.S., Willett, S.D. (Eds.), *Exhumation Processes: Normal Faulting, Ductile Flow, and Erosion*, vol. 154. Geological Society of London, Special Publications, pp. 1–27.
- Ring, U., Johnson, C., Hetzel, R., Gessner, K., 2003. Tectonic denudation of a Late Cretaceous-Tertiary collisional belt: regionally symmetric cooling patterns and their relation to extensional faults in the Anatolide belt of western Turkey. *Geol. Mag.* 140 (4), 421–441.
- Ring, U., Uysal, I.T., Glodny, J., Cox, S.C., Little, T., Thomson, S.N., Stübner, K., Bozkaya, Ö., 2017. Fault-gouge dating in the southern alps, New Zealand. *Tectonophysics* 717, 321–338.
- Rossetti, F., Asti, R., Faccenna, C., Gerdes, A., Lucci, F., Theye, T., 2017. Magmatism and crustal extension: constraining activation of the ductile shearing along the Gediz detachment, Menderes Massif (western Turkey). *Lithos* 282, 145–162.
- Şengör, A.M.C., Satır, M., Akkök, R., 1984. Timing of tectonic events in the Menderes

- Massif, western Turkey: implications for tectonic evolution and evidence for Pan-African basement in Turkey. *Tectonics* 3 (7), 693–707.
- Seyitoğlu, G., Scott, B.C., 1991. Late Cenozoic crustal extension and basin formation in west Turkey. *Geol. Mag.* 128 (2), 155–166.
- Sherlock, S.C., Hetzel, R., 2001. A laser-probe $^{40}\text{Ar}/^{39}\text{Ar}$ study of pseudotachylite from the Tambach Fault Zone, Kenya: direct isotopic dating of brittle faults. *J. Struct. Geol.* 23 (1), 33–44.
- Singleton, J.S., Stockli, D.F., Gans, P.B., Prior, M.G., 2014. Timing, rate, and magnitude of slip on the Buckskin-Rawhide detachment fault, west central Arizona. *Tectonics* 33, 1596–1615.
- Steiger, R.H., Jäger, E., 1977. Subcommission on geochronology: convention on the use of decay constants in geo- and cosmochronology. *Earth Planet. Sci. Lett.* 36, 359–362.
- Thiede, R.C., Arrowsmith, J.R., Bookhagen, B., McWilliams, M.O., Sobel, E.R., Strecker, M.R., 2005. From tectonically to erosionally controlled development of the Himalayan orogen. *Geology* 33 (8), 689–692.
- Torgersen, E., Viola, G., Zwingmann, H., Henderson, I.H.C., 2015. Inclined K-Ar illite age spectra in brittle fault gouges: effects of fault reactivation and wall-rock contamination. *Terra. Nova* 27, 106–113.
- van Hinsbergen, D.J., Kaymakci, N., Spakman, W., Torsvik, T.H., 2010. Reconciling the geological history of western Turkey with plate circuits and mantle tomography. *Earth Planet. Sci. Lett.* 297 (3), 674–686.
- Vanderhaeghe, O., Teyssier, C., Wysoczanski, R., 1999. Structural and geochronologic constraints on the role of partial melting during the formation of the Shuswap metamorphic core complex at the latitude of the Thor-Odin dome, British Columbia. *Can. J. Earth Sci.* 36 (6), 917–943.
- Vanderhaeghe, O., Teyssier, C., McDougall, I., Dunlap, W.J., 2003. Cooling and exhumation of the Shuswap metamorphic core complex constrained by $^{40}\text{Ar}/^{39}\text{Ar}$ thermochronology. *Geol. Soc. Am. Bull.* 115 (2), 200–216.
- Viola, G., Zwingmann, H., Mattila, J., Käpyaho, A., Nova, Terra, 2013. K-Ar illite age constraints on the Proterozoic formation and reactivation history of a brittle fault in Fennoscandia. *Tectonics* 25, 236–244.
- Viola, G., Scheiber, T., Fredin, O., Zwingmann, H., Margreth, A., Knies, J., 2016. Deconvoluting complex structural histories archived in brittle fault zones. *Nat. Commun.* 7, 13448. <https://doi.org/10.1038/ncomms13448>.
- Viola, G., Torgersen, E., Mazzarini, F., Musumeci, G., van der Lelij, R., Schönenberger, J., Garofalo, P.S., 2018. New constraints on the evolution of the inner northern Apennines by K-Ar dating of late Miocene-Early Pliocene compression on the island of Elba, Italy. *Tectonics* 37, 3229–3243.
- Vrolijk, P., van der Pluijm, B.A., 1999. Clay gouge. *J. Struct. Geol.* 21 (8–9), 1039–1048.
- Wagner, G.A., van den Haute, P., 1992. *Fission-track Dating*. Kluwer Academic Publishers, pp. 285.
- Webber, S., Norton, K.P., Little, T.A., Wallace, L.M., Ellis, S., 2018. How fast can low-angle normal faults slip? Insights from cosmogenic exposure dating of the active Mai’iu fault, Papua New Guinea. *Geology* 46 (3), 227–230.
- Wernicke, B.P., Axen, G.J., 1988. On the role of isostasy in the evolution of normal fault systems. *Geology* 16 (9), 848–855.
- Whitney, D.L., Teyssier, C., Rey, P., Buck, W.R., 2013. Continental and oceanic core complexes. *Geol. Soc. Am. Bull.* 125, 273–298 3,4.
- Wolf, R.A., Farley, K.A., Kass, D.M., 1998. Modeling of the temperature sensitivity of the apatite (U-Th)/He thermochronometer. *Chem. Geol.* 148, 105–114.
- Wolf, R., Hetzel, R., Dunkl, I., Bröcker, M., Xu, Q., Anzckiewicz, A.A., 2019. High-angle normal faulting at the Tangra Yumco graben (southern Tibet) since ~15 Ma. *J. Geol.* 127 (1), 15–36.
- Wölfler, A., Kurz, W., Danišák, M., Rabitsch, R., 2010. Dating of fault zone activity by apatite fission track and apatite (U-Th)/He thermochronometry: a case study from the Lavanttal fault system (Eastern Alps). *Terra. Nova* 22 (4), 274–282.
- Wölfler, A., Glotzbach, C., Heineke, C., Nilius, N.P., Hetzel, R., Hampel, A., Akal, C., Dunkl, I., Christl, M., 2017. Late Cenozoic cooling history of the central Menderes Massif: timing of the Büyükk Menderes detachment and the relative contribution of normal faulting and erosion to rock exhumation. *Tectonophysics* 717, 585–598.
- Wu, G., Lavier, L.L., 2016. The effects of lower crustal strength and preexisting midcrustal shear zones on the formation of continental core complexes and low-angle normal faults. *Tectonics* 35, 2195–2214.
- Yilmaz, Y., Genç, S.C., Gürer, F., Bozcu, M., Yilmaz, K., Karacik, Z., Altunkaynak, S., Emas, A., 2000. When did the western Anatolian grabens begin to develop? In: In: Bozkurt, E., Winchester, J.A., Piper, J.D.A. (Eds.), *Tectonics and Magmatism in Turkey and Surrounding Regions*, vol. 173. Geological Society of London, Special Publications, pp. 353–384.
- Zaun, P.E., Wagner, G.A., 1985. Fission-track stability in zircons under geological conditions. *Nucl. Tracks* 10, 303–307.
- Zwingmann, H., Mancktelow, N., 2004. Timing of Alpine fault gouges. *Earth Planet. Sci. Lett.* 223 (2–4), 415–425.
- Zwingmann, H., Mancktelow, N., Antognini, M., Lucchini, R., 2010. Dating of shallow faults – new constraints from the AlpTransit tunnel site (Switzerland). *Geology* 38 (6), 487–490.
- Zwingmann, H., Han, R., Ree, J.H., 2011. Cretaceous reactivation of the Deokpori Thrust, Taebaeksan Basin, South Korea, constrained by K-Ar dating of clayey fault gouge. *Tectonics* 30 (5), 5015. <https://doi.org/10.1029/2010TC002829>.